

Impact of biofilm on the ship propulsion characteristics and the speed reduction

Andrea Farkas¹, Soonseok Song², Nastia Degiuli^{1,*}, Ivana Martić¹, Yigit Kemal Demirel²

¹University of Zagreb, Faculty of Mechanical Engineering and Naval Architecture, Ivana Lučića 5, Zagreb, Croatia

²Department of Naval Architecture, Ocean and Marine Engineering, University of Strathclyde, 100 Montrose Street, Glasgow, G4 0LZ, UK

*nastia.degiuli@fsb.hr

Abstract

Ship fuel consumption and the greenhouse gas emissions in the service are affected by various factors, including waves, wind, biofouling, corrosion, confined water. One of the operational measures for the reduction of the fuel consumption is the optimization of the maintenance schedule, but lack of information related to the potential benefits of the application of this measure represents an important barrier. Therefore, the prediction of the impact of biofouling on ship hydrodynamic characteristics is important. In this paper, a numerical model based on Reynolds Averaged Navier-Stokes (RANS) equations, which allows the prediction of the impact of biofilm on the ship propulsion characteristics is proposed. Roughness function models representing surface conditions of biofilm fouling were employed within the wall function of the CFD software. Thereafter, a detail analysis of the impact of biofilm on the propulsion characteristics and the flow around full-scale containership is presented. This study has demonstrated that the occurrence of biofilm should not be ignored and that the presence of biofilm can cause extremely detrimental effects on ship hydrodynamic characteristics. Thus, it is shown that the biofilm can cause a significant increase in delivered power and consequently an increase in fuel consumption or a decrease in ship speed, contradicting the often ignoring of the biofilm presence on the ship hull.

Keywords:

CFD; biofilm; propulsion characteristics; container ship; speed reduction; biofouling; roughness effect

Introduction

Biofouling is the unwanted growth of microorganisms, plants, algae or animals on wetted surfaces, which leads to functional, financial and environmental drawbacks. It can be considered as a process which occurs in several steps. Firstly, a conditioning film is formed, then it is followed by the adhesion of bacteria and algal cells, which form a biofilm. After the formation of biofilm, the accumulation of diatoms colonies, macroalgae and protozoa spores occurs, thus forming a microfouling along with biofilm. Lastly, macrofouling, which is consisted of both soft and hard fouling, occurs. These stages can be consecutive, happen parallelly, or at the same time (Nurioglu et al., 2015). The rate of biofouling is affected by several factors including duty cycle of a ship (immobile periods, ship speed, route duration and

ship movement patterns) and environmental factors (salinity, nutrients, temperature) (Koboević et al., 2019). The mitigation of biofouling on the wetted surfaces is usually provided through the application of antifouling (AF) coatings (Tezdogan and Demirel, 2014, Stojanović et al., 2019). As AF coatings have a limited service life and cannot be applied or provide adequate protection to all parts of an underwater hull surface, biofouling occurs in between dry-docking periods (Woods et al., 2012). Therefore, regardless of the duty cycle, biofouling occupies wetted surfaces, but due to different duty cycles, different fouling communities can be present. Thus, container ships, which represent ships with relatively high speed and short immobile periods during loading and unloading of cargo, are typically fouled with biofilm and algal communities (Davidson et al., 2009). On the other hand, such ships which have long immobile periods, (e.g. drillship or naval vessel) are often not only fouled with microfouling but also with macrofouling. The hull and propeller conditions and the presence of fouling on their surfaces can bring a significant impact on the ship propulsion characteristics. For some typical merchant vessels in between dry-docking periods, deterioration of hull and propeller performance can result in a 15-20 % loss in the overall propulsive efficiency, which corresponds to a 15-20 % increase in fuel consumption if ship speed remains constant (IMO, 2011). As fuel cost represents 60 – 70 % of the entire operational cost and since hull and propeller fouling cause increases in fuel consumption, the analysis of the fouling level and its influence on the ship performance is crucial for shipping companies (Park et al., 2018). An accurate assessment of the impact of biofouling on the propulsion characteristics is necessary for the optimization of the maintenance schedule. Therefore, there is an increasing number of shipowners that are willing to invest in tools, which will give them the insights related to this impact (van Ballegooijen and Helsloot, 2019). The investigation related to the impact of biofouling on the propulsion characteristics can be classified into different approaches. Thus, there are statistical studies based on the measured data, which are attempting to determine this impact (Adland et al., 2018, Gundermann and Dirksen, 2016). Also, there are studies in which this investigation is carried out for a certain ship, or for few ships, in between dry dockings and after the detailed analysis of measured results, the authors make conclusions (Tarelko, 2014., Coraddu et al., 2019). The important document related to hull and propeller performance monitoring is (ISO 19030, 2016). ISO 19030 is relatively simple and robust approach, which defines performance values (PV) and performance indicators (PI). Even though the approach is based on the actual measurements during ship operation, the approach has several drawbacks. Thus, the filtering of the measured data is rather strict and if the wind force exceeds an upper limit of Beaufort 4 during the measurements, measured data should be discarded. Since most of the current monitoring approaches do not use continuous monitoring, many data are lost due to this filtering, which is inopportune. Another disadvantage is that ISO 19030 does not take into account swell, i.e. only wind waves are considered in this filtering. Thus, waves generated by the swell, i.e. waves generated at the different location and time, do not correspond to the actual wind condition and should be filtered as well (Bertram, 2016). Also, as the measured data is collected during sailing conditions which significantly vary from test run conditions, i.e. the measured data is scattered, and hence the measured data should be corrected (Koboević et al., 2019). This is particularly difficult, as there is no practical approach for quantification of the required added power in waves for performance monitoring (Bertram, 2016). Additional drawbacks including problems correlated with variations of reported average values, unintentional errors as well as an intentional false reporting of the noon reports are presented and discussed in (Tzamaloukas et al., 2018). Despite these drawbacks, ISO 19030 procedure still represents the current best practice for performance monitoring (Bertram, 2017).

Another approach is based on the wall similarity hypothesis, which states that velocity defect profiles are the same in the outer layer for smooth and rough surface since roughness effects are limited to the inner layer (Flack et al., 2007). This hypothesis is valid for all rough surfaces which have the roughness within the inner layer (Schultz et al., 2003). Flack et al., (2007) have presented that this hypothesis is valid for the ratio of the boundary layer thickness to equivalent sand roughness height (δ/k_s) up to 5.5. Thus, the roughness effects are limited to the inner layer and it brings a downward shift of the mean velocity in the log-law region, which

is called the roughness function (ΔU^+). Drag characterization of a rough surface means finding the velocity decrement caused by the frictional drag of the surface as a function of the roughness Reynolds number (k^+). The roughness function, $\Delta U^+ = f(k^+)$, is a different for every surface.

Once ΔU^+ for a certain roughness type is determined, it can be used for predicting the frictional drag of any arbitrary body covered with that roughness type (Yeginbayeva et al., 2019). Several methods for the drag characterization are presented in (Yeginbayeva et al., 2019), including boundary layer measurements for a flat plate in the water tunnel, floating element force balance measurements, towing tank measurements of a flat plate, measurements in pipes, measurements in the rectangular channels and measurements using rotating disks and cylinders. Yeginbayeva et al. (2019) concluded that the flow channel facility, i.e. rectangular channels has the most advantages for the drag characterization and that facility for drag characterization should achieve levels of shear stress (τ_w) which correspond to the ones at ship hulls.

The effect of a certain surface condition on the resistance characteristics can be determined using ΔU^+ and a similarity law analysis (Demirel^a et al., 2017, Monty et al., 2016, Demirel et al., 2019) or through the implementation of ΔU^+ in CFD simulations (Demirel^b et al., 2017, Farkas^b et al., 2018, Speranza et al., 2019, Song^c et al., 2019, Farkas et al., 2019). The merit of using CFD simulations is that it allows determination of the roughness effect on every resistance component (Song^c et al., 2019, Farkas et al., 2019). What is more, this approach can predict the variation of friction velocity (U_τ) over the immersed body and thus a variation of k^+ as well (Demirel^b et al., 2017), while similarity law scaling method assumes only one k^+ value for the whole immersed body at a certain Reynolds number (Rn).

Regardless of the applied approach, the determination of the effect of biofouling on the resistance and propulsion characteristics is as equally important as the improvement of the energy efficiency of existing ships through the application of new AF coatings, since it can demonstrate the importance of hull and propeller cleaning (Owen et al., 2018, Song^b et al., 2019, Song^a et al., 2019). Therefore, the International Towing Tank Conference (ITTC) has advised researchers to propose new formulae or methods based on the experimental data to determine this effect (ITTC, 2011). The attachment of the biofilm on the ship hull is inevitable regardless of the applied AF coating (Hydrex Underwater Technology, 2010). Fouling with the biofilm, i.e. slime, is often ignored since it is believed that the presence of slime does not have an important effect on the resistance and propulsion characteristics. This is evident from the definition of Antifouling Performance Index (API) proposed by Hempel, which ranges from 0 to 100%. Thus, even if 50 % of the wetted surface is covered with slime, API is equal to 90%, meaning that AF coating has excellent performance (Silva et al., 2019). Due to the presence of

biofilm, two scenarios can occur, either delivered power (P_D) will increase if the ship speed is maintained, or ship speed will decrease if P_D is maintained as for smooth surface condition.

In this paper, the impact of biofilm on the propulsion characteristics of a full-scale containership is investigated numerically and the aforementioned scenarios are evaluated. To the best of the authors' knowledge, the effect of biofilm on the propulsion characteristics using Computational Fluid Dynamics (CFD) is investigated in this study for the first time. This study was carried out using numerical simulations based on viscous flow with ΔU^+ proposed in (Farkas^b et al., 2018) implemented within wall function of the commercial software package STAR-CCM+. Therefore, this investigation can be considered as a continuation of studies presented in (Farkas^b et al., 2018, Farkas et al., 2019). Verification study is performed, and both grid and time step numerical uncertainties are estimated. Initially, validation study is performed by comparing the numerically obtained resistance, open water and propulsion characteristics for smooth surface condition with the extrapolated towing tank measurements presented in the literature. Thereafter, the CFD model has been modified in order to account the effect of biofilm through the implementation of ΔU^+ proposed in (Farkas^b et al., 2018). These ΔU^+ have been validated and their applicability in the determination of ship hydrodynamic characteristics is discussed in (Farkas^b et al., 2018, Farkas et al., 2019). The obtained results demonstrate the impact of biofilm on the increase in P_D if the ship speed is maintained and the reduction of ship speed if P_D is maintained as for smooth surface condition.

Methodology

Governing equations

Reynolds Averaged Navier-Stokes (RANS) equations are used as a governing equation in this study. The averaged continuity and RANS equations read:

$$\frac{\partial(\rho \bar{u}_i)}{\partial x_i} = 0 \quad (1)$$

$$\frac{\partial(\rho \bar{u}_i)}{\partial t} + \frac{\partial}{\partial x_j} (\rho \bar{u}_i \bar{u}_j + \overline{\rho u'_i u'_j}) = -\frac{\partial \bar{p}}{\partial x_i} + \frac{\partial \bar{\tau}_{ij}}{\partial x_j} \quad (2)$$

where ρ is the density, \bar{u}_i is the averaged velocity vector, $\overline{\rho u'_i u'_j}$ is the Reynolds stress tensor, \bar{p} is the mean pressure and $\bar{\tau}_{ij}$ is the mean viscous stress tensor given as:

$$\bar{\tau}_{ij} = \mu \left(\frac{\partial \bar{u}_i}{\partial x_j} + \frac{\partial \bar{u}_j}{\partial x_i} \right) \quad (3)$$

where μ is the dynamic viscosity.

$k - \omega$ Shear Stress Transport (SSTKO) turbulence model with wall functions is used for closing RANS equations. Finite Volume Method (FVM) is used for the discretization of governing equations, while Volume Of Fluid (VOF) method is used for modelling the free surface. Governing equations are solved in a segregated manner, convective terms are discretized using

the second-order upwind convection scheme while the first-order scheme is used for the temporal discretization.

As said before, drag characterization of a rough surface means finding ΔU^+ as a function of k^+ . k^+ is given as:

$$k^+ = \frac{kU_\tau \rho}{\mu} \quad (4)$$

where k represents the roughness length scale. As k cannot be measured directly, the goal of the roughness studies is to find a relation between k and some easily measured surface properties (Monty et al, 2016). Schultz et al. (2015) have proposed a new effective roughness length scale for biofilm (k_{eff}) which depends on the biofilm height (k) and percentage of the surface coverage with the biofilm (%SC) as follows:

$$k_{eff} = 0.055k\sqrt{\%SC} \quad (5)$$

In order to determine the effect of biofilm on the propulsion characteristics, ΔU^+ models proposed by Farkas^b et al. (2018) are used. As %SC presents a critical parameter for fundamental ΔU^+ behaviour, three ΔU^+ models were proposed (Farkas^b et al., 2018):

- for %SC > 25%:

$$\Delta U^+ = \begin{cases} \frac{1}{\kappa} \ln(0.27767k^+) & \text{for } k^+ \geq 3.61 \\ 0 & \text{for } k^+ < 3.61 \end{cases} \quad (6)$$

- for 10% < %SC < 25%:

$$\Delta U^+ = \begin{cases} \frac{1}{\kappa} \ln(1.14492 + 0.0988k^+) & \text{for } k^+ \geq 4.5 \\ 0 & \text{for } k^+ < 4.5 \end{cases} \quad (7)$$

- for %SC < 10%:

$$\Delta U^+ = \begin{cases} \frac{1}{\kappa} \ln(1.06492 + 0.05332k^+) & \text{for } k^+ \geq 4 \\ 0 & \text{for } k^+ < 4 \end{cases} \quad (8)$$

where κ is the von Karman constant equal to 0.42.

A comprehensive clarification on the wall function approach used for the assessment of the effect of biofilm on propulsion characteristics is shown in (Farkas^b et al., 2018). Details about the utilization of ΔU^+ are presented in (Demirel et al., 2014).

Approach

In order to develop a CFD model which can simulate the effect of biofilm on the propulsion characteristics several steps should be carried out. Thus, using ΔU^+ values and corresponding

k^+ values obtained in Turbulent Channel Flow (TCF) facility for flat plates covered with biofilm (Schultz et al., 2015), ΔU^+ models were proposed and implemented within wall function of CFD model (Farkas^b et al., 2018). Thereafter, the proposed ΔU^+ models were validated through numerical simulations of the flow in TCF facility, where model scale flat plates covered with biofilm were placed (Farkas^b et al., 2018), and the comparison with frictional resistance coefficients (C_F) obtained in (Schultz et al., 2015). Furthermore, numerical simulations of viscous flow around full-scale flat plate representing ship were performed and the obtained results are validated with the results obtained using Granville similarity law scaling method (Farkas^b et al., 2018). Once ΔU^+ are validated, they can be used for the prediction of the effect of biofilm on the resistance and propulsion characteristics. The impact of biofilm on the resistance characteristics and nominal wake, using the proposed ΔU^+ , is investigated by Farkas et al. (2019). This investigation is carried out by application of proposed ΔU^+ models in CFD simulations of a towed ship. In order to assess the impact of biofilm on propulsion characteristics, firstly proposed ΔU^+ models are applied in CFD simulations of Open Water Test (OWT). Thus the impact of biofilm on the thrust (K_T) and torque (K_Q) coefficients, as well as on the open water efficiency (η_o) is assessed for several advance coefficients (J). As shown by Owen et al. (2018), similar results are obtained using Moving Reference Frame (MRF) method and sliding mesh method, the latter is computationally more expensive. Therefore, in this study MRF method is applied and CFD simulations of OWT are carried out as steady simulations.

The impact of biofilm on propulsion characteristics is determined using the proposed ΔU^+ models in CFD simulations of self-propulsion test (SPT). In this paper, the body force propeller method is utilized for modelling the effects of the propeller and thus the CFD simulations of SPT are carried out without resolving the propeller geometry. For more details regarding the application of MRF and body force propeller method, reference may be given to (Farkas^a et al., 2018). The first step is the validation of the obtained results for the smooth surface condition. Thus, both numerically obtained open water and self-propulsion characteristics are validated against the extrapolated towing tank results published in the literature (NMRI, 2015). Thereafter, CFD model is modified, i.e. proposed ΔU^+ models are implemented within wall function and CFD simulations are performed for several surface conditions fouled with biofilm. The obtained results present the impact of biofilm on the propulsion characteristics, i.e. on the operating point of a marine propeller. The change in certain propulsion characteristic (φ) is obtained by the following equation:

$$\Delta\varphi = 100\% \cdot \frac{\varphi_R - \varphi_S}{\varphi_S} \quad (9)$$

where index R denotes the rough surface condition and S the smooth surface condition. Changes in propulsion characteristics were calculated for eight different surface conditions which included fouling with biofilm, Table 1. In Table 1 fouling rating scale (FR) along with fouling percentages (FP) is given for each investigated surface condition based on NSTM rating (Naval Ships' Technical Manual, 2002). The presented surface conditions are studied in the way that certain surface condition is present both at the hull and propeller.

Table 1. Studied surface conditions

Surface condition	k -biofilm height, μm	%SC - percentage of surface coverage, %	k_{eff} - roughness length scale for biofilm, μm	ΔU^+ model	NSTM rating (Naval Ships' Technical Manual, 2002)
R1	100	50	39	Eq. (6)	FR 10, 50%
R2	500	50	195	Eq. (6)	FR 20, 50%
R3	100	25	27.5	Eq. (6)	FR 10, 25%
R4	500	25	137.5	Eq. (6)	FR 20, 25%
R5	100	15	21.3	Eq. (7)	FR 10, 15%
R6	500	15	106.5	Eq. (7)	FR 20, 15%
R7	100	5	12.3	Eq. (8)	FR 10, 5%
R8	500	5	61.5	Eq. (8)	FR 20, 5%

Open water and self-propulsion characteristics

Open water characteristics define characteristics of a marine propeller which operates in uniform flow with a steady load and include K_T , K_Q and η_o which are obtained for several J . K_T and K_Q are non-dimensional coefficients defines as follows:

$$K_T = \frac{T}{\rho n^2 D^4} \quad (10)$$

$$K_Q = \frac{Q}{\rho n^2 D^5} \quad (11)$$

where T is the propeller thrust, Q is the propeller torque, n is propeller rate of revolution and D is the propeller diameter.

Non-dimensional J is given as:

$$J = \frac{v_A}{nD} \quad (12)$$

where v_A is the speed of the advance.

η_o can be determined as follows:

$$\eta_o = \frac{J}{2\pi} \cdot \frac{K_T}{K_Q} \quad (13)$$

Delivered power to the propeller, P_D , in order to sail at a certain ship speed is calculated as:

$$P_D = 2\pi n Q \quad (14)$$

Due to different conditions behind the ship and in the uniform flow, at the same J propeller provides different K_Q values. The difference in P_D when operating in uniform flow and behind the ship is accounted through relative rotative efficiency:

$$\eta_R = \frac{K_{QO}}{K_{Qb}} \quad (15)$$

where K_{QO} is the torque coefficient obtained in OWT, while K_{Qb} is the torque coefficient obtained in SPT.

The velocities of the flow over the hull surface are increased due to propeller operation behind the ship. Therefore, the local pressure field over the aft part of the hull surface is reduced, causing the increase in resistance. Thus, T is always higher than the total resistance (R_T) and this increase in resistance is accounted with the thrust deduction factor defined as follows:

$$t = 1 - \frac{R_T}{T} \quad (16)$$

Wake fraction (w) is given as:

$$w = 1 - \frac{v_A}{v} \quad (17)$$

where v is the ship speed. Thus, w can be considered as the loss of the axial velocity in the propeller disk plane when compared to v and expressed as a proportion of v .

Once w and t are known, the hull efficiency can be easily determined:

$$\eta_H = \frac{1-t}{1-w} \quad (18)$$

The overall propulsive efficiency can be determined as follows:

$$\eta_P = \eta_H \eta_O \eta_R \quad (19)$$

Numerical setup

Geometry, computational domain, boundary conditions

The effect of biofilm on open water and propulsion characteristics is studied for a marine propeller KP 505 and Kriso Container Ship (KCS) (NMRI, 2015). Parameters of KP 505 along with the main particulars of KCS are shown in Table 2.

Table 2. Parameters of KP 505 and main particulars of KCS

Parameter	KP 505	Particular	KCS
D	7.9 m	L_{pp}	230 m
P	7.505 m	L_{wl}	232.5 m
A_E/A_O	0.8	B	32.2 m

d/D	0.18	T	10.8 m
Z	5	Δ	53382.8 t
Direction of rotation	right	S	9539 m ²
Blade section	NACA 66	C_B	0.6505
n	1.5 rps	V	24 kn

KCS body plan can be seen in Figure 1, while propeller drawing of the model propeller KP 505 is shown in Figure 2.

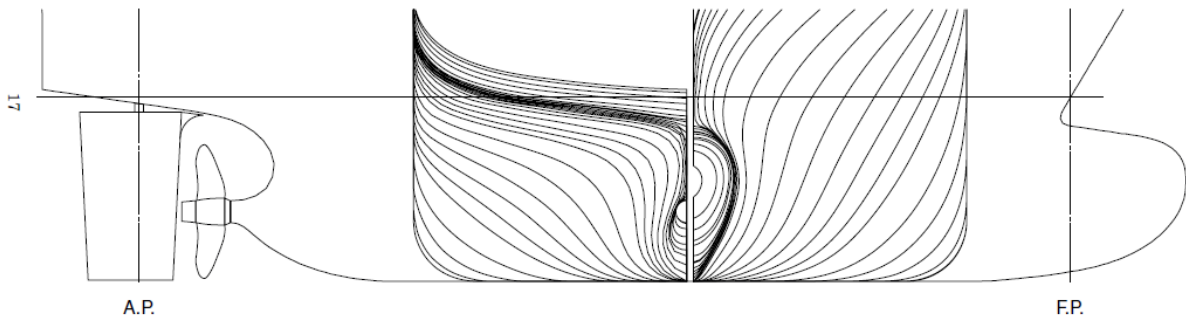


Figure 1. Hull lines of KCS (NMRI, 2015)

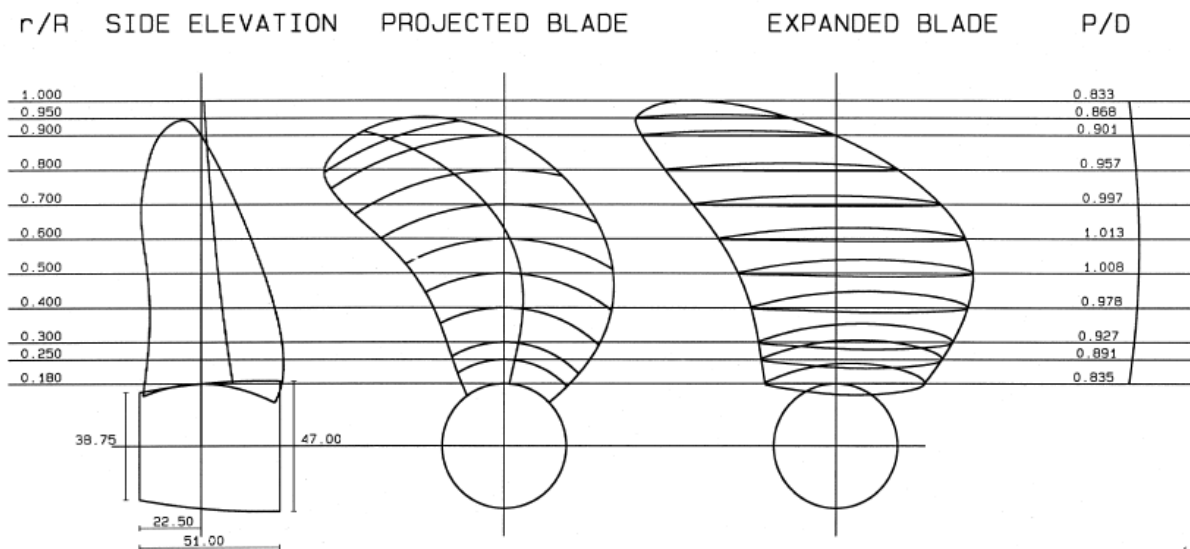


Figure 2. Propeller drawing of KP 505 model (in geometry scale $\lambda = 31.6$) (NMRI, 2015)

In order to obtain the propulsion characteristics of a ship, resistance, OWT and SPT should be performed. An extensive study regarding the impact of biofilm on the resistance characteristics and nominal wake of two full-scale merchant ships is presented by Farkas et al. (2019). For more details regarding the computational domain, applied boundary conditions as well as domain discretization for numerical simulations of resistance tests, reference may be given to (Farkas et al., 2019).

In this paper, OWT and SPT for full-scale KCS are carried out for several surface conditions covered with biofilm. Thereafter, the impact of biofilm on propulsion characteristics is assessed. For numerical simulations of OWT and SPT, the domain boundaries are placed sufficiently far in order to prevent their effect on the results (Farkas^a et al., 2018, Owen et al., 2018) as shown in Figure 3. The applied boundary conditions in OWT are velocity inlet for inlet boundary, pressure outlet for outlet boundary, no-slip wall for propeller, cap and shaft and slip wall for lateral surface of a domain. The applied boundary conditions in numerical simulations of SPT are pressure outlet for outlet boundary, no-slip wall for ship and rudder surfaces and velocity inlet for all other boundaries.

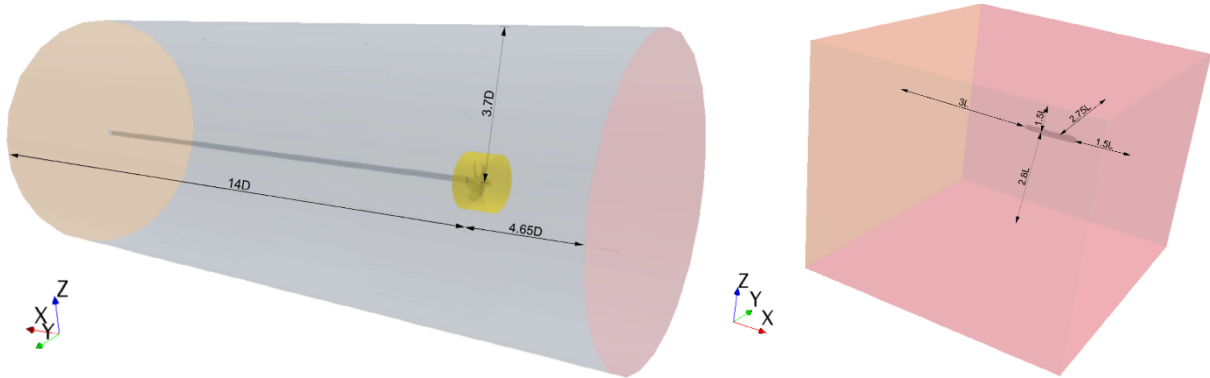


Figure 3. Computational domain for OWT (left) and SPT (right)

In order to prevent wave reflections from domain boundaries, VOF wave damping is applied in numerical simulations of SPT for the outlet, inlet, left and right-side boundaries. This damping is performed using the damping function implemented within STAR-CCM+ (Farkas et al., 2017) and damping length is set to L_{pp} .

Computational domains are discretized utilizing unstructured hexahedral mesh. Special care is given to near wall mesh generations. The y^+ values at the first cell near the wall are kept above 30 and k^+ (Demirel^b et al., 2017). The mesh for OWT is refined in the region around propeller, where isotropic mesh refinement extends $0.6D$ upstream and $2.25D$ downstream. An appropriate demarcation between the suction and pressure side of the propeller is created as the mesh refinement along the leading and trailing edges is made, Figure 4. Thus, a fine mesh for OWT has around 7M cells.

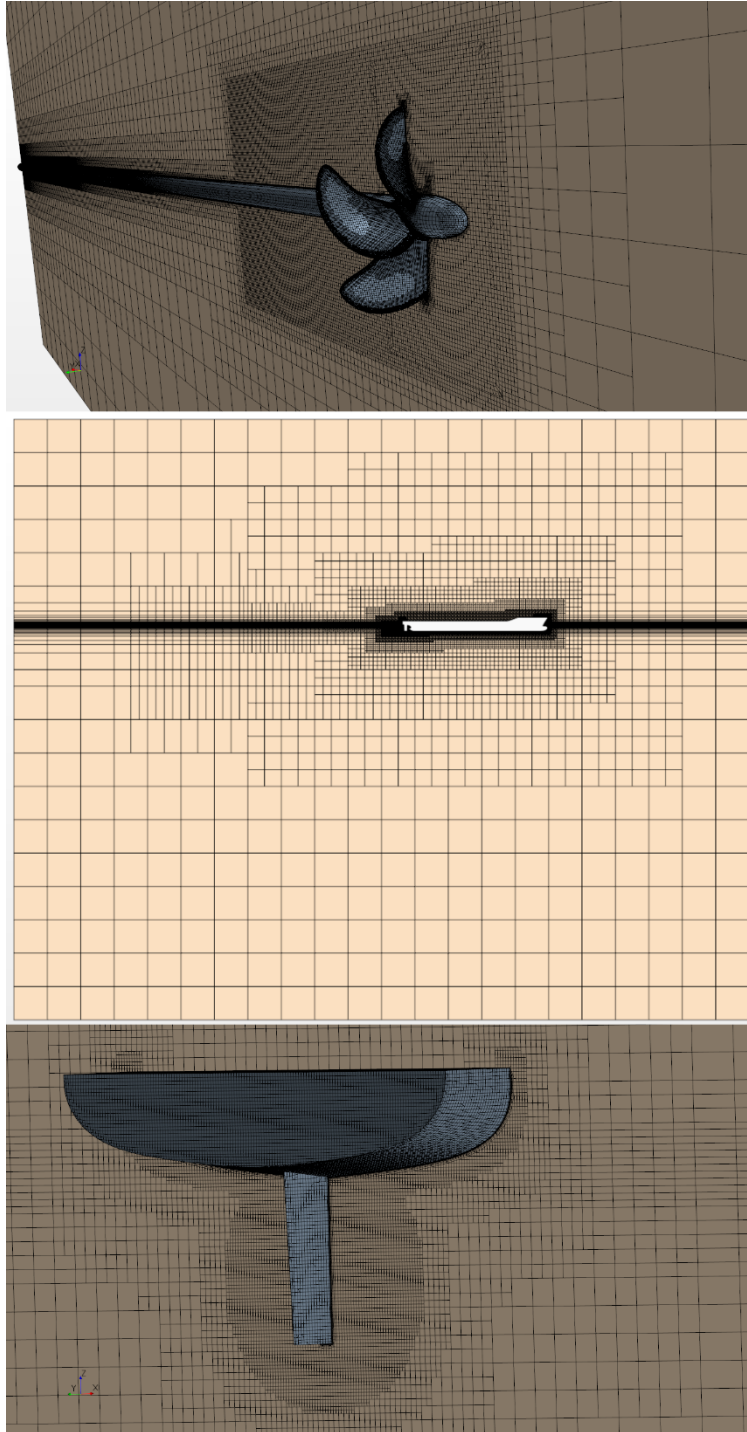


Figure 4. Side view of mesh (top) used for OWT, profile view cross-section of mesh (middle) used in SPT and mesh refinement in stern region (lower) used in SPT

Numerical simulations of OWT are carried out for the full-scale propeller KP 505 at the J range of 0.1-0.8 in a way that n is kept constant, i.e. $n=1.5$ rps and v_A is changed through iterations. Simulations of OWT are carried out as steady MRF simulations. For each J , 2000 iterations are performed before the change to the next J .

The mesh for SPT is refined in order to capture the Kelvin wake around the free surface, near the hull surface, as well as in the region where virtual disk is located, as shown in Figure 4. The refinement in the region where virtual disk is located is made as a cylindrical refinement with

the radius equal to $1.05 D$ and length equal to $9 D$, i.e. $5 D$ downstream and $4 D$ upstream from propeller, as done in (Farkas^a et al., 2018). Furthermore, cell size at hull surface is set as $1/1000 L_{pp}$, thus allowing very fine discretization of hull geometry.

The main parameters of the virtual disk model are shown in Table 3. More details regarding the virtual disk model and details of its application can be found in (Farkas^a et al., 2018).

Table 3. The main parameters of virtual disk model

Parameter	
inner radius	propeller hub radius (d)
outer radius	propeller radius (R)
thickness	propeller thickness
inflow plane radius	$1.1R$
inflow plane offset	$1.1D$ towards the bow from the half of virtual disk thickness

Numerical simulations of SPT are performed with the time step as the one used in numerical simulations of resistance tests (Farkas et al., 2019), i.e. $T/200$, where T is defined as the ratio between ship length and speed. Thrust is selected as an operating point input option rather than propeller rotation rate. Self-propulsion point is obtained once total resistance and thrust are equal and when these forces became steady. It should be noted that these forces in numerical simulations of SPT oscillated around the average value, with oscillation amplitude lower than 0.5% of the total resistance/thrust value, i.e. these forces became steady (Farkas et al., 2017).

Verification study

Verification study is performed for grid size and time step for numerical simulations of OWT and SPT to determine adequate grid spacing and time step, as well as to estimate the numerical uncertainties of numerical simulations using the Grid Convergence Index (GCI) method. Obviously, as the OWT simulations are carried as steady simulations, only a grid convergence study is performed for OWT. GCI method can be used for the determination of uncertainties which occur due to grid spacing and time step errors and is often used in the literature (Song^c et al., 2019, Farkas et al., 2019, Tezdogan et al., 2015, Terziev et al., 2018). It should be noted that the grid convergence study is performed for three different meshes with the finest time step, while time step convergence study is performed for three different time steps with the finest grid.

The apparent order of method is determined by the following equations:

$$p_a = \frac{1}{\ln(r_{21})} \left| \ln \left| \frac{\varepsilon_{32}}{\varepsilon_{21}} \right| + q(p_a) \right| \quad (20)$$

$$q(p_a) = \ln \left(\frac{r_{21}^{p_a} - s}{r_{32}^{p_a} - s} \right) \quad (21)$$

$$s = \text{sign} \left(\frac{\varepsilon_{32}}{\varepsilon_{21}} \right) \quad (22)$$

where r_{21} and r_{32} are refinement factors, $\varepsilon_{21} = \phi_2 - \phi_1$, $\varepsilon_{32} = \phi_3 - \phi_2$ and ϕ_i is the solution obtained with i -th input parameter. For temporal convergence study refinement factors are equal to 2. For grid convergence study refinement factors are equal to $r_{21} = 1.264$ and $r_{32} = 1.255$ in SPT, as fine mesh has around 8.5 M cells, medium mesh around 4.2 M cells and coarse mesh around 2.1 M cells, while in OWT are equal to $r_{21} = 1.117$ and $r_{32} = 1.134$, as fine mesh has around 7.1 M cells, medium mesh around 5.1 M cells and coarse mesh around 3.5 M cells.

The extrapolated solution is determined by the equation (23), while the approximate relative error and extrapolated relative error are calculated with equations (24) and (25) respectively.

$$\phi_{ext}^{21} = \frac{r_{21}^{p_a} \phi_1 - \phi_2}{r_{21}^{p_a} - 1} \quad (23)$$

$$e_a^{21} = \left| \frac{\phi_1 - \phi_2}{\phi_1} \right| \quad (24)$$

$$e_{ext}^{21} = \left| \frac{\phi_{ext}^{21} - \phi_1}{\phi_{ext}^{21}} \right| \quad (25)$$

GCI for fine input parameter is calculated as follows:

$$GCI_{fine}^{21} = \frac{1.25e_a^{21}}{r_{21}^{p_a} - 1} \cdot 100\% \quad (26)$$

Simulation uncertainty can be determined as follows:

$$U_{SN} = \sqrt{U_I^2 + U_G^2 + U_T^2} \quad (27)$$

where U_I is the iteration uncertainty, which is considered to be negligible in comparison with grid uncertainty (U_G) and time step uncertainty (U_T).

Grid dependence study is performed for two surface conditions: smooth (S) and R2. For OWT, grid convergence study is performed at $J=0.7$. In addition, T and Q are used as key variables for the calculation of the spatial discretization error, as shown in Table 4. For SPT, P_D , n , T and J are used as key variables for the calculation of the spatial discretization error, Table 4.

Table 4. Grid dependence study, OWT and SPT

OWT	T , kN				
Surface condition	ϕ_1	ϕ_2	ϕ_3	ϕ_{ext}^{21}	GCI_{fine}^{21} , %
S	1622.11	1621.12	1623.04	1623.3	0.092
R2	1562.98	1562.70	1564.40	1563.05	0.006
OWT	Q , kNm				
Surface condition	ϕ_1	ϕ_2	ϕ_3	ϕ_{ext}^{21}	GCI_{fine}^{21} , %
S	2085.42	2085.39	2088.92	2085.42	0.000
R2	2155.59	2158.92	2164.87	2149.10	0.376

SPT	n , rpm				
Surface condition	ϕ_1	ϕ_2	ϕ_3	ϕ_{ext}^{21}	GCI_{fine}^{21} , %
S	99.341	99.686	100.982	99.225	0.146
R2	104.159	104.288	105.346	104.143	0.020
SPT	P_D , MW				
Surface condition	ϕ_1	ϕ_2	ϕ_3	ϕ_{ext}^{21}	GCI_{fine}^{21} , %
S	24.624	25.321	26.744	24.010	3.121
R2	33.569	33.995	35.105	33.323	0.914
SPT	T , kN				
Surface condition	ϕ_1	ϕ_2	ϕ_3	ϕ_{ext}^{21}	GCI_{fine}^{21} , %
S	1810.89	1877.34	1903.77	1763.46	3.274
R2	2288.84	2314.23	2381.15	2226.21	3.421
SPT	J				
Surface condition	ϕ_1	ϕ_2	ϕ_3	ϕ_{ext}^{21}	GCI_{fine}^{21} , %
S	0.7293	0.7215	0.7196	0.7319	0.453
R2	0.6701	0.6655	0.6647	0.6760	1.100

Relatively low numerical uncertainties of fine mesh in the prediction of T and Q are obtained for both surface conditions with the highest numerical uncertainty equal to 0.376% obtained for R2 in the prediction of Q . It should be noted that remaining numerical simulations of OWT are carried out using fine mesh and that results obtained using fine mesh are used as an input for SPT. As shown in Table 4, the numerical uncertainties of fine mesh in the prediction of n and J are relatively low for both surface conditions, i.e. it is lower than 0.15% for n and lower than 1.1% for J . The numerical uncertainties of fine mesh in the prediction of P_D and T are somewhat higher but are still below 3.5%. It should be noted that remaining simulations were performed using fine mesh.

Time step convergence study is performed using three different time steps for two surface conditions, S and R2 in SPT. P_D , n , T and J are used as key variables for the calculation of the temporal discretization error, Table 5.

Table 5. Time step convergence study, SPT

Surface condition	n rpm				
	ϕ_1	ϕ_2	ϕ_3	ϕ_{ext}^{21}	GCI_{fine}^{21} , %
S	99.341	99.577	99.697	99.094	0.311
R2	104.159	104.293	104.384	103.871	0.346
Surface condition	P_D , MW				
	ϕ_1	ϕ_2	ϕ_3	ϕ_{ext}^{21}	GCI_{fine}^{21} , %
S	24.624	24.918	25.058	24.355	1.367
R2	33.569	33.740	33.837	33.342	0.846
Surface condition	T , kN				

	ϕ_1	ϕ_2	ϕ_3	ϕ_{ext}^{21}	$GCI_{fine}^{21}, \%$
S	1810.89	1827.69	1833.25	1802.58	0.574
R2	2288.84	2298.95	2303.81	2279.48	0.511
Surface condition	J				
	ϕ_1	ϕ_2	ϕ_3	ϕ_{ext}^{21}	$GCI_{fine}^{21}, \%$
S	0.7293	0.7279	0.7269	0.7321	0.479
R2	0.6701	0.6691	0.6689	0.6702	0.028

As can be seen from Table 5, the numerical uncertainty of fine time step in the prediction of n is relatively low for both surface conditions, i.e. it is lower than 0.35%. Numerical uncertainties of fine time step in the prediction of T and J are only slightly higher (below 0.58% for T and below 0.48% for J). The highest numerical uncertainties for fine time step are obtained in the prediction of P_D , however the obtained numerical uncertainties are lower than 1.37%. It should be noted that temporal uncertainties are lower than spatial uncertainties in the prediction of P_D , n , T and J . All remaining simulations are performed using the fine time step.

The obtained simulation uncertainties for SPT are shown in Table 6.

Table 6. The obtained simulation uncertainties, SPT

Key variable/Surface condition	$U_{SN}, \%$	
	S	R2
n	0.341	0.361
P_D	3.407	1.247
T	3.323	3.459
J	0.659	1.101

As can be seen from Table 6, the simulation uncertainties are higher for the prediction of T and P_D than for n and J , but are still below 3.5%. Also, it can be seen that U_{SN} for R2 are similar to U_{SN} for smooth surface condition or even lower. Therefore, it can be concluded that the implementation of ΔU^+ within the wall function did not lead to higher uncertainties in the prediction of P_D , n , T and J .

Validation study

The modified wall function approach, which includes the implementation of roughness functions for biofilm, defined with equations (6) – (8), is validated by Farkas^b et al. (2018), while the applicability of this approach for the determination of the impact of biofilm on the resistance characteristics and nominal wake is shown in (Farkas et al., 2019). Thus, the obtained total resistance coefficient as well as the nominal wake coefficient at the full scale for the smooth surface condition are validated with the comparison with the extrapolated towing tank results. Satisfactory agreement between the numerical and extrapolated results is achieved with RD between $C_{T,CFD}$ and $C_{T,EX}$ lower than 2.43% and RD between $(1-w_N)_{CFD}$ and $(1-w_N)_{EX}$

lower than 2.18% (Farkas et al., 2019). In this paper, ΔU^+ defined with equations (6) – (8) are implemented in the numerical simulations of OWT and SPT. Numerically obtained open water characteristics for smooth surface conditions are validated with the experimental results (NMRI, 2105). Also, the numerically obtained self-propulsion point, i.e. delivered power and propeller rotation rate for the smooth surface condition is validated with the extrapolated results utilizing the experimental data of (Kim et al., 2001, NMRI, 2015). The experimental data is extrapolated to full-scale using ITTC 1957 Performance Prediction Method. Thus, the self-propulsion point of the ship is obtained once the difference between the total resistance and thrust is equal to skin friction correction. At the self-propulsion point of ship, propeller revolution rate for full-scale ship is obtained in accordance with Froude similarity law:

$$n_s = \frac{n_M}{\sqrt{\lambda}} \quad (28)$$

where n_M is the propeller revolution rate for ship model.

Delivered power to the propeller at full scale can be calculated as follows:

$$P_D = 2\pi\rho n_s^3 K_Q D^5 \quad (29)$$

Relative deviations between numerically (φ_{CFD}) and experimentally (φ_{EX}) obtained results are calculated by:

$$RD = \frac{\varphi_{CFD} - \varphi_{EX}}{\varphi_{EX}} \cdot 100\% \quad (30)$$

Numerically obtained OWT results for the smooth surface condition are validated with the towing tank results published in the literature (NMRI, 2015), Figure 5. It should be noted that towing tank experiments are performed for a propeller in model scale with the assumption that OWT characteristics are independent of Rn , i.e. that propeller diameter in model scale is sufficiently large. As can be seen from Figure 5, a satisfactory agreement is achieved between the results of CFD and experiment. A similar agreement between OWT characteristics obtained utilizing CFD and experimental values is obtained by Castro et al. (2011), where the authors also obtained slightly higher values of η_0 using CFD when compared to experimental η_0 .

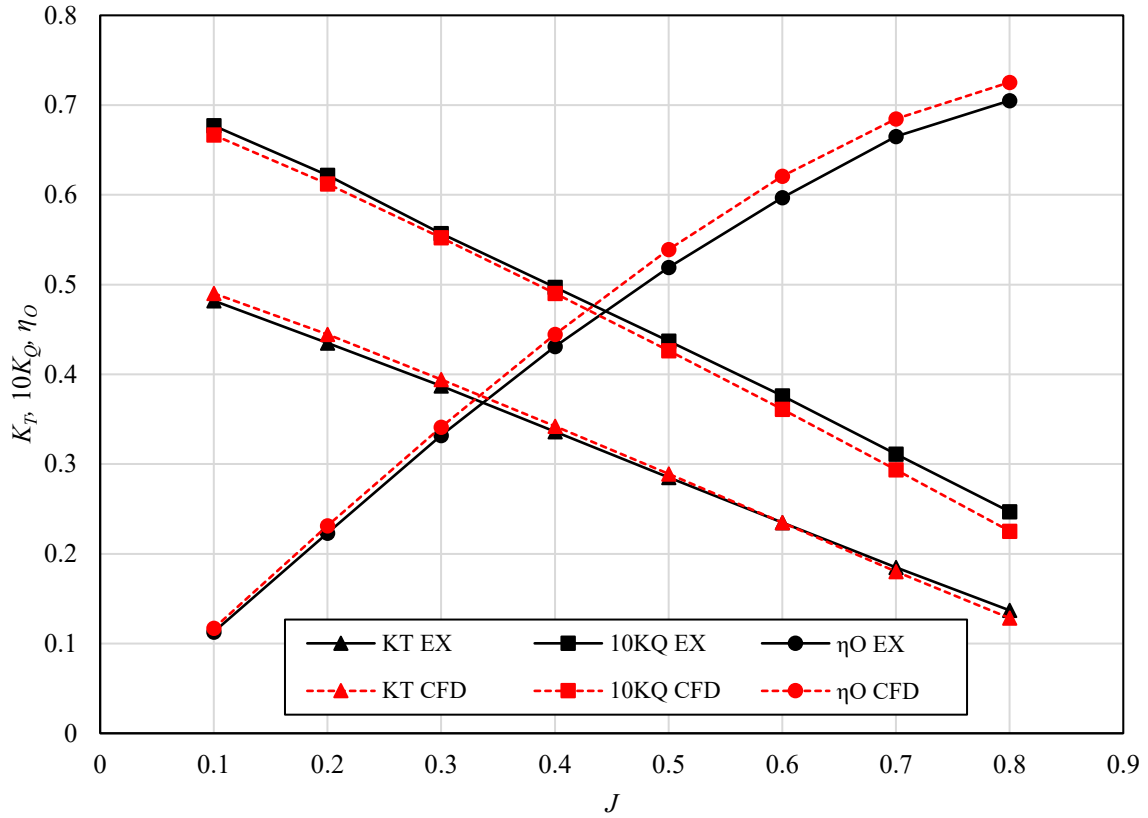


Figure 5. Validation of the obtained OWT characteristics

The numerical simulation of SPT at the full scale for the smooth surface condition is validated by a comparison with the extrapolated towing tank values. The obtained results from SPT are summarized along with the extrapolated towing tank results in Table 7. The propulsion characteristics are obtained using resistance, open water and self-propulsion test results. Also, the results published in (Castro et al., 2011) are shown in Table 7, as well, where the propeller was discretized and the overset mesh was used.

Table 7. Propulsion characteristics obtained for full scale KCS and smooth surface condition

Characteristic	EX	CFD	<i>RD</i> , %	(Castro et al., 2011)	<i>RD</i> , %
K_T	0.170	0.165	-2.763	0.166	-2.353
$10K_Q$	0.288	0.274	-5.033	0.296	2.778
n , rpm	101.398	99.341	-2.029	104.186	2.750
$1-t$	0.853	0.867	1.613	0.842	-1.325
$1-w$	0.792	0.773	-2.440	0.794	0.189
J	0.728	0.729	0.179	0.714	-1.896
η_O	0.682	0.700	2.674	0.683	0.103
η_R	1.011	1.002	-0.906	1.057	4.580
η_P	0.740	0.787	6.343	0.766	3.459

As can be seen from Table 7, satisfactory agreement between the numerical and extrapolated values is achieved as RD are relatively low and similar to the ones reported in (Castro et al., 2011). Thus, the obtained propulsion characteristics have relative deviation lower than 2.8% from the extrapolated values at the self-propulsion point. The only exceptions are K_Q for which RD is around 5% and η_p for which RD is equal to 6.34%. As mentioned by Farkas^a et al. (2018), RD between numerically obtained and extrapolated propulsion characteristics can be attributed to various aspects, including an insufficient accuracy of the nominal wake prediction, underestimations of K_T and K_Q at higher J in OWT, as well as consequent overestimations of η_0 in OWT. Also, RD can be associated with a modelling error, due to the modelling of the propeller effect, rather than discretizing the propeller itself, as well as a numerical error related with the number of the cells and temporal discretization. An important aspect related to these RD can be attributed to the extrapolation procedure and ideally the obtained numerical results should be compared to the measured values at the full-scale.

Results

Impact of biofilm on the propulsion characteristics

After the verification and validation studies, the impact of biofilm on the propulsion characteristics is assessed using equation (9). This impact is determined using the fine mesh and fine time step. As said before, due to the presence of the roughness, either delivered power will increase if the ship speed is kept constant, or ship speed will decrease if delivered power is kept the same as for smooth surface condition. Both the scenarios are analysed and presented in this section.

Impact of biofilm on the propulsion characteristics for the constant ship speed

In this subsection the impact of biofilm on the delivered power at the constant ship speed is shown, and the importance of the assessment of the impact of biofilm on the delivered power rather than on the effective power is highlighted. Firstly, the effect of biofilm on the open water characteristics is shown in Tables 8-10.

Table 8. Impact of biofilm on K_T

J	S	R1	R2	R3	R4	R5	R6	R7	R8
0.1	0.4902	0.4856 (-0.933%)	0.4808 (-1.916%)	0.4865 (-0.760%)	0.4820 (-1.678%)	0.4882 (-0.411%)	0.4854 (-0.980%)	0.4893 (-0.177%)	0.4876 (-0.524%)
0.2	0.4445	0.4403 (-0.961%)	0.4357 (-1.982%)	0.4411 (-0.778%)	0.4369 (-1.730%)	0.4427 (-0.418%)	0.4401 (-1.009%)	0.4438 (-0.177%)	0.4422 (-0.536%)
0.3	0.3944	0.3904 (-1.008%)	0.3861 (-2.106%)	0.3912 (-0.814%)	0.3872 (-1.839%)	0.3927 (-0.438%)	0.3902 (-1.066%)	0.3937 (-0.186%)	0.3922 (-0.562%)
0.4	0.3423	0.3385 (-1.086%)	0.3344 (-2.311%)	0.3393 (-0.871%)	0.3354 (-2.013%)	0.3407 (-0.468%)	0.3383 (-1.155%)	0.3416 (-0.197%)	0.3402 (-0.600%)
0.5	0.2889	0.2854 (-1.214%)	0.2813 (-2.631%)	0.2861 (-0.966%)	0.2823 (-2.288%)	0.2874 (-0.514%)	0.2852 (-1.297%)	0.2883 (-0.213%)	0.2870 (-0.664%)
0.6	0.2348	0.2314 (-1.437%)	0.2274 (-3.140%)	0.2321 (-1.137%)	0.2284 (-2.728%)	0.2334 (-0.603%)	0.2312 (-1.540%)	0.2342 (-0.247%)	0.2329 (-0.781%)
0.7	0.1804	0.1776 (-1.579%)	0.1738 (-3.645%)	0.1782 (-1.214%)	0.1748 (-3.130%)	0.1794 (-0.559%)	0.1773 (-1.709%)	0.1801 (-0.182%)	0.1790 (-0.780%)
0.8	0.1284	0.1254 (-2.305%)	0.1217 (-5.251%)	0.1261 (-1.810%)	0.1226 (-4.534%)	0.1272 (-0.946%)	0.1252 (-2.489%)	0.1279 (-0.385%)	0.1268 (-1.233%)

Table 9. Impact of biofilm on $10K_Q$

J	S	R1	R2	R3	R4	R5	R6	R7	R8
0.1	0.6667	0.6694 (0.416%)	0.6728 (0.925%)	0.6689 (0.330%)	0.6720 (0.796%)	0.6677 (0.155%)	0.6695 (0.426%)	0.6671 (0.063%)	0.6680 (0.208%)
0.2	0.6121	0.6151 (0.483%)	0.6186 (1.062%)	0.6145 (0.389%)	0.6177 (0.921%)	0.6132 (0.186%)	0.6151 (0.498%)	0.6126 (0.080%)	0.6136 (0.248%)
0.3	0.5523	0.5555 (0.580%)	0.5592 (1.242%)	0.5549 (0.470%)	0.5582 (1.077%)	0.5535 (0.226%)	0.5556 (0.591%)	0.5528 (0.095%)	0.5539 (0.299%)
0.4	0.4902	0.4937 (0.714%)	0.4975 (1.488%)	0.4931 (0.584%)	0.4966 (1.296%)	0.4916 (0.285%)	0.4938 (0.725%)	0.4908 (0.121%)	0.4920 (0.374%)
0.5	0.4266	0.4304 (0.900%)	0.4344 (1.834%)	0.4297 (0.741%)	0.4334 (1.600%)	0.4281 (0.369%)	0.4305 (0.912%)	0.4272 (0.160%)	0.4286 (0.481%)
0.6	0.3611	0.3652 (1.147%)	0.3694 (2.324%)	0.3645 (0.947%)	0.3684 (2.031%)	0.3628 (0.476%)	0.3653 (1.163%)	0.3618 (0.208%)	0.3633 (0.618%)
0.7	0.2936	0.2986 (1.710%)	0.3035 (3.365%)	0.2978 (1.428%)	0.3023 (2.974%)	0.2959 (0.782%)	0.2987 (1.738%)	0.2947 (0.363%)	0.2965 (0.977%)
0.8	0.2254	0.2307 (2.354%)	0.2357 (4.585%)	0.2297 (1.947%)	0.2345 (4.036%)	0.2276 (1.003%)	0.2307 (2.391%)	0.2263 (0.435%)	0.2283 (1.296%)

Table 10. Impact of biofilm on η_o

J	S	R1	R2	R3	R4	R5	R6	R7	R8
0.1	0.1170	0.1155 (-1.343%)	0.1137 (-2.815%)	0.1158 (-1.087%)	0.1142 (-2.454%)	0.1164 (-0.565%)	0.1154 (-1.400%)	0.1168 (-0.240%)	0.1162 (-0.731%)
0.2	0.2312	0.2279 (-1.437%)	0.2242 (-3.012%)	0.2285 (-1.163%)	0.2251 (-2.627%)	0.2298 (-0.603%)	0.2277 (-1.500%)	0.2306 (-0.256%)	0.2294 (-0.782%)
0.3	0.3410	0.3356 (-1.579%)	0.3297 (-3.306%)	0.3366 (-1.277%)	0.3311 (-2.885%)	0.3387 (-0.663%)	0.3354 (-1.648%)	0.3400 (-0.281%)	0.3381 (-0.858%)
0.4	0.4445	0.4366 (-1.787%)	0.4279 (-3.744%)	0.4381 (-1.446%)	0.4300 (-3.267%)	0.4412 (-0.750%)	0.4362 (-1.867%)	0.4431 (-0.318%)	0.4402 (-0.971%)
0.5	0.5390	0.5277 (-2.095%)	0.5154 (-4.384%)	0.5299 (-1.694%)	0.5184 (-3.826%)	0.5343 (-0.880%)	0.5272 (-2.189%)	0.5370 (-0.372%)	0.5329 (-1.139%)
0.6	0.6210	0.6051 (-2.555%)	0.5878 (-5.339%)	0.6081 (-2.065%)	0.5920 (-4.665%)	0.6143 (-1.074%)	0.6044 (-2.672%)	0.6181 (-0.454%)	0.6123 (-1.390%)
0.7	0.6846	0.6625 (-3.233%)	0.6382 (-6.782%)	0.6668 (-2.605%)	0.6440 (-5.927%)	0.6755 (-1.330%)	0.6614 (-3.388%)	0.6809 (-0.543%)	0.6727 (-1.740%)
0.8	0.7254	0.6924 (-4.552%)	0.6572 (-9.405%)	0.6987 (-3.685%)	0.6657 (-8.238%)	0.7114 (-1.930%)	0.6909 (-4.766%)	0.7195 (-0.817%)	0.7073 (-2.496%)

As can be seen from Tables 8 and 9, K_T decreases due to the presence of biofilm, while K_Q increases when compared to the smooth surface condition and this is more highlighted as the fouling rate increases. Thus, for the most severe surface condition, R2 (Table 1), the decrease in K_T varies from -1.916% to -5.251% depending on J , while the increase in K_Q varies from 0.925% to 4.585% depending on J . This leads to severe decrease in η_o (Table 10), and for R2, the decrease in η_o varies from -2.815% to -9.405%. For the surface condition with the lowest fouling rate, R7, the decrease in K_T varies from -0.177% to -0.385% depending on J , while the increase in K_Q varies from 0.063% to 0.435% depending on J , which leads to decrease in η_o and this decrease varies from -0.240% to -0.817%. It can be concluded that even though investigated surface conditions can be classified as slime, i.e. soft fouling, the significant detrimental effect of biofilm on the open water characteristics is noticed. This is also observed by Kresic et al. (1983), where the authors showed a tendency of a rapid loss in η_o when only a small amount of initial roughness is present. The decrease in η_o due to the presence of biofilm can be attributed to two aspects; roughness effect on the skin friction and the pressure field.

The presence of biofilm causes the increase in skin friction, i.e. drag coefficient of the blades increases, which leads to an increase in K_Q . The distribution of wall shear stress magnitude on

the smooth and fouled (R2) propeller surface is shown in Figure 6 at $J=0.7$. Due to the presence of biofilm, the wall shear stress magnitude is increased significantly and therefore drag coefficient of the blades increases.

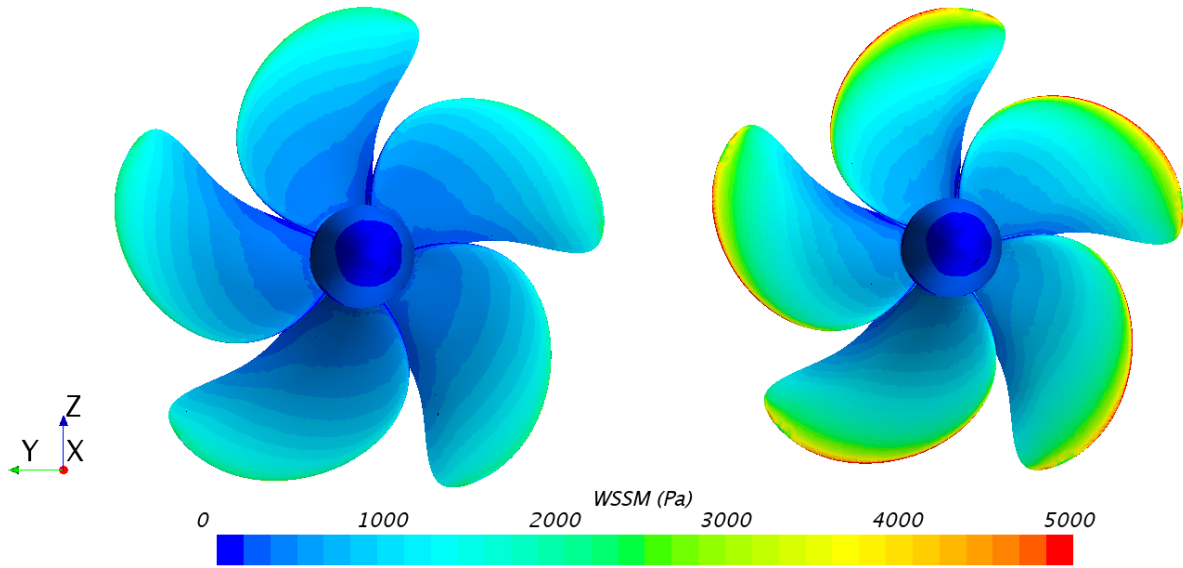


Figure 6. Distribution of wall shear stress magnitude on the smooth (left) and fouled (R2) (right) propeller surface

The pressure field around the propeller can also be attributed to the reduction of η_o . The reduced pressure difference between the pressure and suction sides of the propeller results in decreased lift coefficients of the blade sections and hence decreased K_T , as similarly observed by Song^b et al. (2019). This can be seen in Figure 7, where difference of pressure coefficient along the pressure and suction side of propeller with R2 and smooth surface condition is shown. It should be noted that pressure coefficient is obtained by dividing the pressure with the dynamic pressure defined as $\frac{1}{2}\rho v_R^2$. The resultant velocity of the flow approaching the propeller blade section is obtained as follows:

$$v_R = \sqrt{v_A^2 + (0.7\pi nD)^2} \quad (31)$$

Because of both the increase in K_O and decrease in K_T , η_o is reduced significantly.

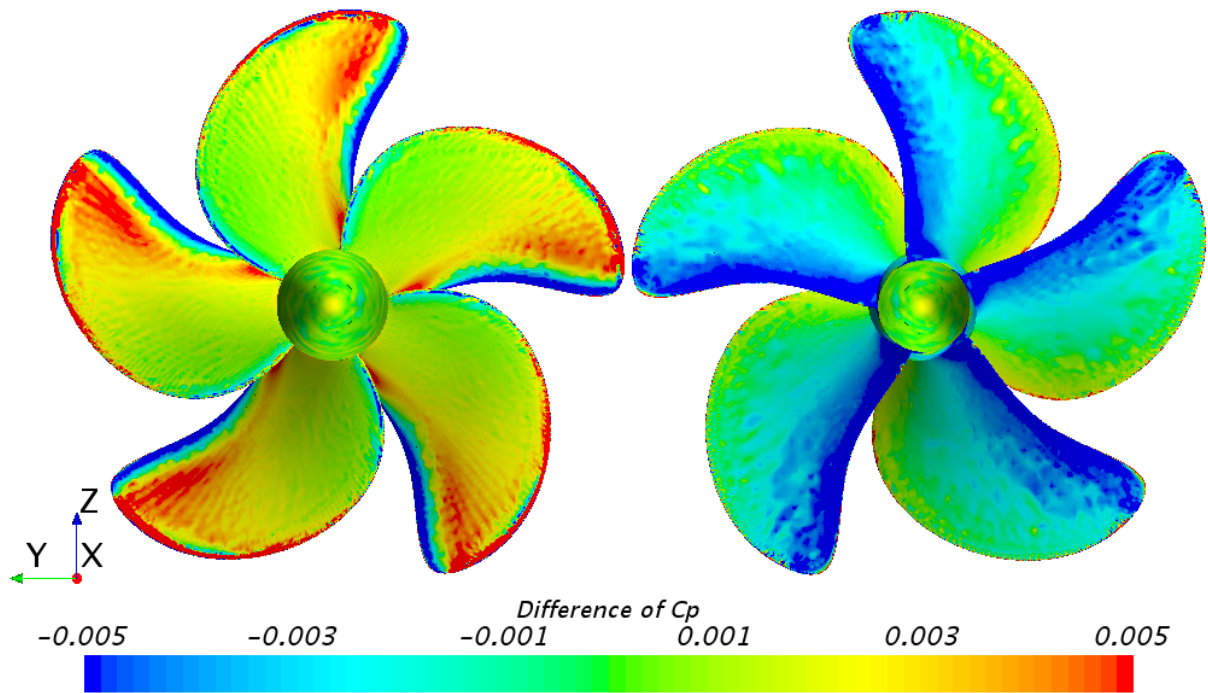


Figure 7. Difference of dynamic pressure coefficient along the pressure side (upper) and suction side of propeller with R2 and smooth surface condition

The changes in K_T and K_Q values due to the biofilm are observed to be larger at higher J (i.e. $J=0.7-0.8$), as shown in Tables 8 and 9. Larger changes in K_T and K_Q values at higher J resulted in a tendency for the higher reduction in η_o at higher J values as shown in Table 10. Therefore, it can be deduced that the ships which operate at higher J will experience a greater reduction in η_o and consequently greater reduction in the performance.

Having carried out OWT, the obtained results are used as an input for Virtual Disk Model. Also, roughness function models are implemented within wall function and thus, SPT is performed for rough hull and propeller surfaces. The impact of biofilm on T , Q , n , J and P_D is shown in Table 11, while the impact of biofilm on the propulsion characteristics is shown in Table 12, i.e. both values and the changes in physical quantities are shown. It should be noted that in Table 11, the impact of biofilm on R_T is shown as well, which is obtained from CFD simulations of a towed ship carried out in (Farkas et al., 2019).

Table 11. The impact of biofilm on T , Q , n , J , P_T and P_D

	S	R1	R2	R3	R4	R5	R6	R7	R8
R_T , kN	1569.6	1711.3 (9.029%)	1973.9 (25.756%)	1669.9 (6.391%)	1915.8 (22.055%)	1633.1 (4.045%)	1755.7 (11.859%)	1577.1 (0.477%)	1653.0 (5.315%)
T , kN	1810.9	1984.2 (9.569%)	2288.8 (26.393%)	1924.2 (6.259%)	2196.8 (21.308%)	1876.4 (3.615%)	2007.2 (10.840%)	1816.0 (0.281%)	1910.9 (5.520%)
Q , kNm	2367.0	2647.0 (11.828%)	3077.6 (30.020%)	2563.9 (8.319%)	2952.2 (24.722%)	2476.3 (4.615%)	2675.7 (13.040%)	2397.2 (1.273%)	2522.1 (6.553%)
n , rpm	99.341	101.242 (1.914%)	104.159 (4.850%)	100.672 (1.340%)	103.288 (3.973%)	100.035 (0.698%)	101.374 (2.046%)	99.462 (0.122%)	100.404 (1.070%)
J	0.7293	0.7061 (-3.187%)	0.6701 (-8.119%)	0.7140 (-2.094%)	0.6801 (-6.744%)	0.7201 (-1.265%)	0.7026 (-3.656%)	0.7280 (-0.177%)	0.7164 (-1.765%)
P_T , MW	17.275	18.676 (8.109%)	21.034 (21.761%)	18.211 (5.418%)	20.319 (17.620%)	17.796 (3.014%)	18.825 (8.975%)	17.315 (0.230%)	18.099 (4.771%)

P_D , MW	24.624	28.063 (13.968%)	33.569 (36.326%)	27.030 (9.770%)	31.932 (29.678%)	25.940 (5.346%)	28.405 (15.354%)	24.968 (1.396%)	26.518 (7.693%)
------------	--------	---------------------	---------------------	--------------------	---------------------	--------------------	---------------------	--------------------	--------------------

As can be seen from Table 11, the impact of biofilm on P_D is detrimental and it causes the increase in P_D from 1.396% for R7 and up to 36.326% for R2. This significant ΔP_D can be attributed to several detrimental effects of biofilm on the resistance and propulsion characteristics. Thus, ΔR_T varies from 0.477% for R7 up to 25.756% for R2, and ΔT varies from 0.281% for R7 up to 26.393% for R2. These increases are quite similar, meaning that the impact of biofilm on $1-t$ is minimal, as can be seen from Table 12. Thus, it can be seen that $\Delta(1-t)$ is lower than 0.92%, which backs up hypothesis made by Townsin et al. (1985), where the authors assumed that the effect of roughness on t is negligible. However, it should be noted that the investigated fouling condition in this paper represents a soft fouling and further studies with hard fouling should be performed in order to assume that the effect of any kind of roughness on t is negligible. For example, in (Song^a et al., 2019), the authors have found that the presence of barnacles, which represent hard fouling, causes the increase in $1-t$. Therefore, additional studies should be performed before drawing any definite conclusions. Differently to the effect of biofilm on t , the effect of biofilm on $1-w$ is significant and detrimental. Thus, it causes decreases of $1-w$ from -0.055% to -3.663% for R7 and R2, respectively. This decrease can be attributed to slower flow around the area where propeller is operating and the flow slows down due to thicker boundary layer, as hull is fouled (Figure 11). The decrease of $1-w$ has beneficial effect on η_H , equation (18). Thus, η_H increases due to the presence of biofilm from 0.251% for R7 up to 3.279% for R2. Regardless of this, the decrease of $1-w$ has detrimental effect on η_p and P_D . Namely, the decrease of $1-w$ means that flow around the propeller is slower and therefore the propeller operating point is changed when compared with the smooth hull surface. Thus, J is decreased because of the presence of biofilm as the speed of advance is lower. What is more, J is also decreased because of the higher n , as can be seen from Table 11 and this decrease ranges from -0.177% for R7 up to -8.119% for R2. The decrease in J is unfavourable, as KP505 operates with J which is lower than J for which η_o function has a maximum value. Therefore, the decrease in J causes the decrease in η_o and this decrease is larger than the increase in η_H , which can be seen from Table 12, where the decrease in η_o ranges from -0.710% for R7 up to -10.472% for R2. It is evident that the surface roughness, besides detrimental effect on the open water characteristics, has detrimental effect on the propeller operating point, which can lead to equally meaningful effect on η_o as worsening of the open water characteristics can have.

The effect of biofilm on η_R is negligible and $\Delta\eta_R$ is lower than 0.45% for all investigated surface conditions as was assumed by Townsin et al. (1985). As said before, further studies should be performed with other types of roughness in order to make a proper conclusion about the roughness effect on η_R . Since, the decrease in η_o is higher than the increase in η_H , η_P decreases due the presence of biofilm and this decrease ranges from -0.907% for R7 up to -7.753% for R2.

As can be seen from Table 11, both n and Q increase due to the presence of biofilm, which leads to significant increases in P_D . Thus, the increase in n ranges from 0.122% for R7 up to 4.850% for R2, while the increase in Q ranges from 1.273% for R7 up to 30.020% for R2.

Table 12. The impact of biofilm on propulsion characteristics

	S	R1	R2	R3	R4	R5	R6	R7	R8
$1-w$	0.7727	0.7624 (-1.335%)	0.7444 (-3.663%)	0.7666 (-0.782%)	0.7492 (-3.038%)	0.7682 (-0.575%)	0.7597 (-1.685%)	0.7723 (-0.055%)	0.7672 (-0.714%)
$1-t$	0.8668	0.8625 (-0.493%)	0.8624 (-0.504%)	0.8678 (0.124%)	0.8721 (-0.616%)	0.8704 (0.415%)	0.8747 (0.920%)	0.8685 (0.196%)	0.8651 (-0.194%)
η_H	1.1218	1.1313 (0.853%)	1.1585 (3.279%)	1.1320 (0.913%)	1.1640 (3.768%)	1.1329 (0.996%)	1.1515 (2.649%)	1.1246 (0.251%)	1.1276 (0.523%)
η_R	1.0018	1.0001 (-0.169%)	0.9995 (-0.234%)	0.9994 (-0.242%)	1.0000 (-0.188%)	1.0004 (-0.148%)	1.0000 (-0.181%)	0.9974 (-0.448%)	1.0002 (-0.166%)
η_O	0.7002	0.6653 (-4.982%)	0.6269 (-10.472%)	0.6742 (-3.722%)	0.6363 (-9.126%)	0.6858 (-2.062%)	0.6627 (-5.360%)	0.6953 (-0.710%)	0.6823 (-2.555%)
η_P	0.7869	0.7528 (-4.334%)	0.7259 (-7.753%)	0.7627 (-3.079%)	0.7407 (-5.879%)	0.7772 (-1.235%)	0.7631 (-3.029%)	0.7798 (-0.907%)	0.7696 (-2.208%)

The importance of the determination of the roughness effect on P_D , rather than on P_E , i.e. R_T , can be noticed from the Table 11. Thus, a significantly higher increase in P_D when compared to the increase in R_T is obtained. ΔP_D is higher than ΔP_E due to the detrimental effect of biofilm on the open water characteristics, as well as due to the detrimental effect on the propeller operating point. On the other hand, ΔP_T are lower than ΔP_E , i.e. ΔR_T and this can be attributed to the fact that the impact of biofilm on $1-t$ value is rather low, while the impact of biofilm on $1-w$ and consequently on v_A is noticeable and detrimental. Therefore, due to the presence of biofilm, ΔT is similar to ΔR_T , Table 11, while v_A is reduced and thus ΔP_T are lower than ΔP_E . The obtained results indicate that the effect of biofilm should not be ignored as it can lead to a substantial worsening of ship resistance and propulsion characteristics and consequently to a high increase in P_D .

Impact of biofilm on the speed reduction for the constant P_D

As the obtained increases in P_D are relatively large it could be worthy to investigate the impact of biofilm on the speed reduction for the constant P_D . Namely, due to the presence of roughness ship operators can reduce the ship speed, rather than having a large fuel penalty keeping the ship speed constant. In order to estimate speed reduction due to the presence of biofilm, additional numerical simulations of SPT are performed for each surface condition at two reference speeds: the design speed (24 knots) and the slow streaming speed (19 knots). Thereafter, a second-order polynomial is fitted to the obtained data and finally achievable speed is determined for constant value of P_D , equal to the one obtained for smooth surface condition. For the design speed, P_D is equal to 24.624 MW and for the slow steaming speed P_D is equal to 10.535 MW. The obtained speed reductions due to the presence of biofilm are shown in Table 13.

Table 13. Impact of biofilm on the speed reduction for constant P_D

Reference speed	24 kn (design speed)		19 kn (slow steaming speed)	
Surface condition	v , kn	Δv , %	v , kn	Δv , %
R1	23.15	-3.541	18.48	-2.760
R2	21.98	-8.411	17.37	-8.567
R3	23.39	-2.546	18.66	-1.807
R4	22.34	-6.932	17.79	-6.378
R5	23.65	-1.455	18.79	-1.082
R6	23.05	-3.949	18.28	-3.812
R7	23.91	-0.384	19.00	0.000
R8	23.51	-2.040	18.72	-1.492

As can be seen from Table 13, the obtained speed reduction for constant P_D ranges from -0.384% to -8.411% for R7 and R2 respectively for the design speed, while the obtained speed reduction ranges from 0% to -8.567% for R7 and R2 respectively for a slow steaming speed. For the design speed for R5, R7 and R8 speed reduction is lower than 0.5 kn, for R1, R3 and R6, speed reduction is lower than 1 kn, while for R2 and R4 speed reduction is higher than 1 kn. For the slow steaming speed for R1, R3, R5, R7 and R8, speed reduction is around or lower than 0.5 kn, for R6 is lower than 1 kn, while for R2 and R4 speed reduction is higher than 1 kn. As can be seen from Table 13, for surface conditions with lower fouling rates for slow steaming speed, the speed reduction is quite low, or even negligible. Although the contribution of the frictional resistance in the total resistance is expected to be larger at lower speeds, since C_F for fully rough flow regime is independent of Rn , the speed reductions due to the biofilms are observed to be larger for the design speed. This can be attributed to the fact that at 19 kn, U_τ values along the ship hull are lower than U_τ values at 24 kn. As k^+ is a function of U_τ and for same surface condition defined with k_{eff} , k^+ values along the ship hull at 19 kn are lower than the ones obtained at 24 kn. It should be noted that the flow around ship hull for low values of k^+ is in the hydraulically smooth regime and ΔU^+ is equal to 0. Figure 8 shows the obtained k^+ distribution in SPT for R7 at 19 kn. As can be seen from Figure 8, k^+ values along the ship hull are mostly below the threshold value, which is for this surface condition equal to 4, i.e. if $k^+ < 4$, the flow is in the hydraulically smooth regime. Obviously, these areas where k^+ is above 4 cover only small portion of wetted surface, i.e. they did not have any effect on ΔP_D . For other surface conditions these areas, i.e. areas above threshold value, where the flow is no longer in hydraulically smooth regime, are larger and therefore they have some impact on ΔP_D . However, only for surface condition R2 which represents a surface condition with the highest k_{eff} , Δv at 19 kn are higher than Δv at 24 kn. For this surface condition, obviously the fact that the portion of R_F in R_T is higher at 19 kn than at 24 kn and therefore ΔR_T is higher at 19 kn than at 24 kn has surpassed the fact that ΔU^+ values are lower at 19 kn than at 24 kn.

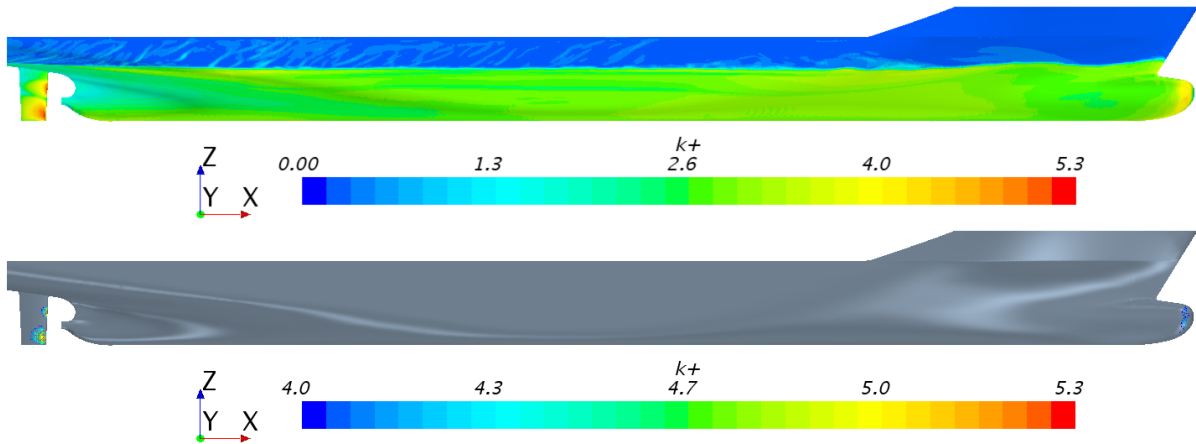


Figure 8. k^+ distribution obtained in SPT for R7 at 19 kn

The impact of biofilm on Q and n obtained at different ship speeds is shown in Figure 9. At the reduced speed, due to the presence of biofilm, even though P_D is the same as for smooth surface condition, Q will be higher than at the design speed and for the smooth surface condition, but n will be reduced. It should be noted that if the engine cannot provide sufficient Q , either P_D would have to be reduced according to the engine characteristic curve, or additional gear system would be needed, which is not desirable. For a fouled hull and propeller, the propeller curve is moved to the left towards lower values of n , i.e. propeller curve behaves as heavy loaded propeller curve (Carlton, 2007). The impact of biofilm on P_D can be noticed at different ship speeds in Figure 9, where a significant increase in P_D can be noticed for surface conditions R2 and R4. Following this, ΔP_D for surface conditions R6 and R1 is more than two times lower when compared to the ΔP_D for R2 and for surface conditions R3, R8 and R5 ΔP_D is even lower. Lastly, ΔP_D for R7 is almost negligible as this surface condition has the lowest value of k_{eff} .

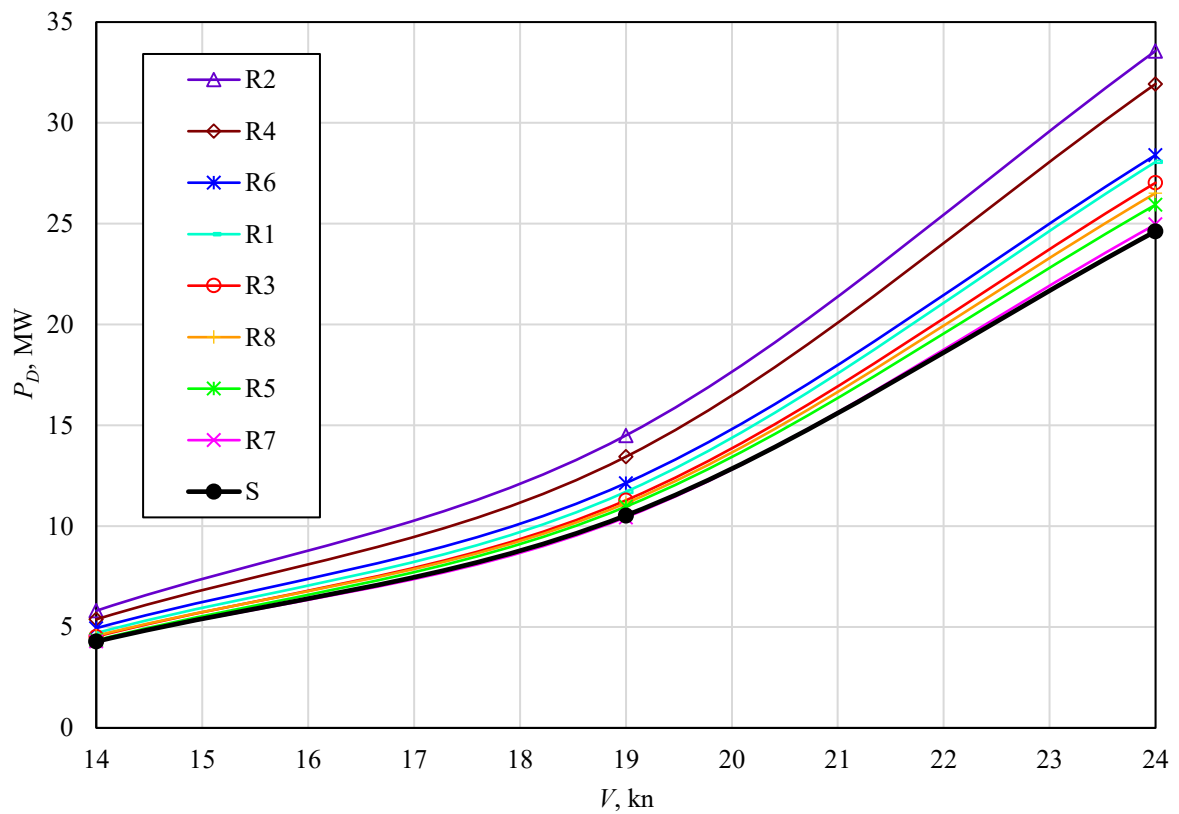
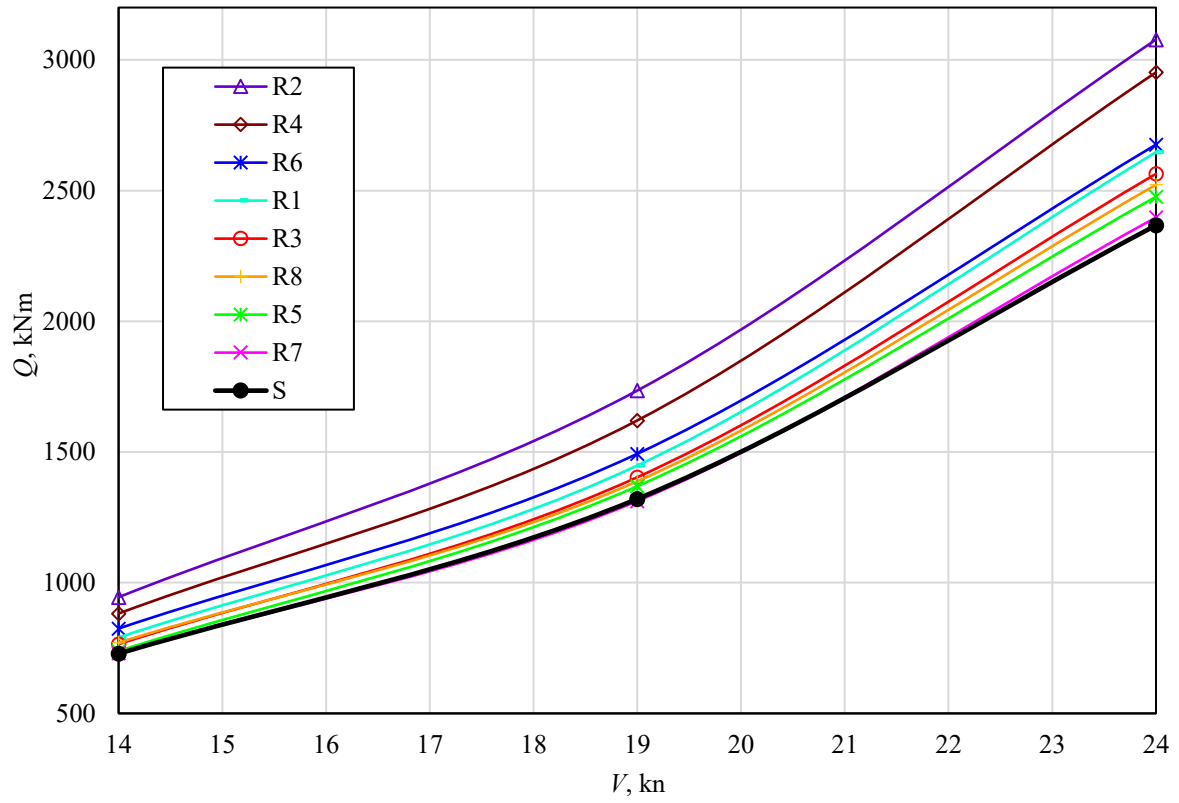


Figure 9. The impact of biofilm on Q (upper) and P_D (lower) obtained at different ship speeds

Impact of biofilm on the flow around ship hull

In this subsection, the flow characteristics around the fouled and smooth ship hulls are presented. Figure 10 shows the contours of the turbulent kinetic energy and velocity magnitude at the midship of KCS for smooth surface condition and R2 in SPT. It is evident from Figure 10 that the presence of biofilm causes the increase in turbulent kinetic energy, while decreasing the velocity magnitude near the surface, which suggests increases in the boundary layer thickness. Figure 11 shows the boundary layers at location $x=30$ m for smooth surface condition and R2. As can be seen from Figure 11, the presence of biofilm resulted in the increase of boundary layer thickness and due to this increase C_F will increase as well (Song^e et al., 2019, Flack et al., 2007, Schultz, 2000). The boundary layer is represented using the slices of axial velocity contours which are limited to $v_x / v_{ship} = 0.99$. This increase in turbulence eventually results in increased wall shear stress (τ_w) as shown in Figure 12.

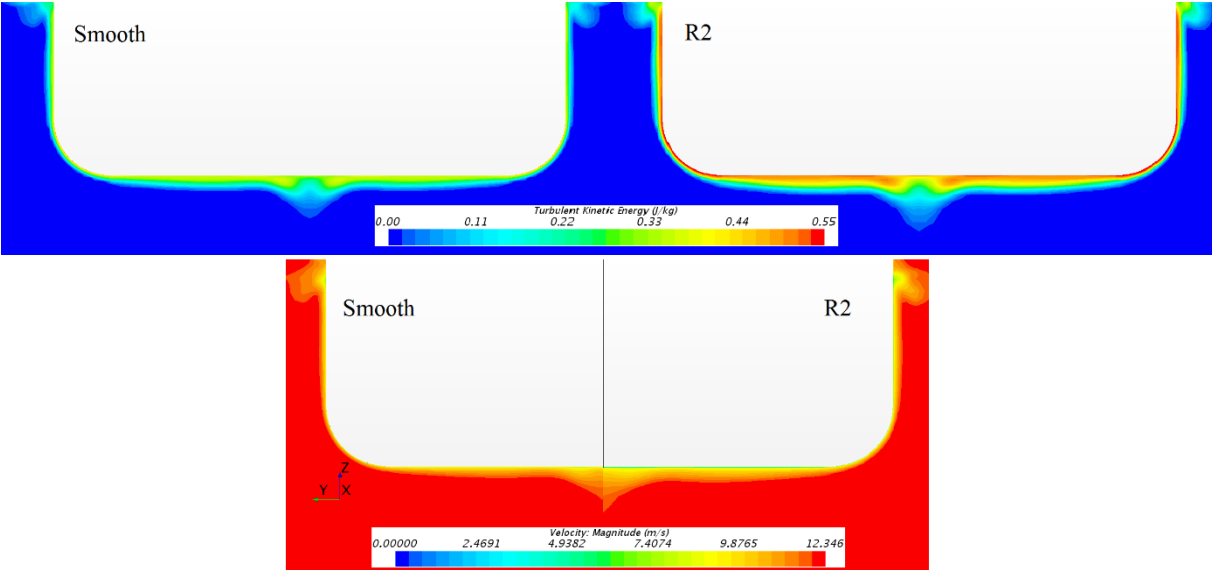


Figure 10. Contours of turbulent kinetic energy (upper) and velocity magnitude (lower) at the midship of the KCS for smooth (left) and R2 (right)

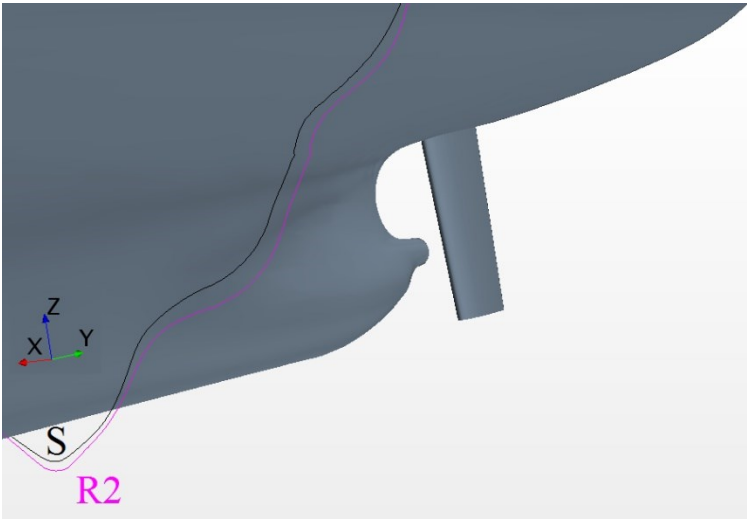


Figure 11. Boundary layers at location $x=30$ m for smooth surface condition (black line) and R2 (purple line)

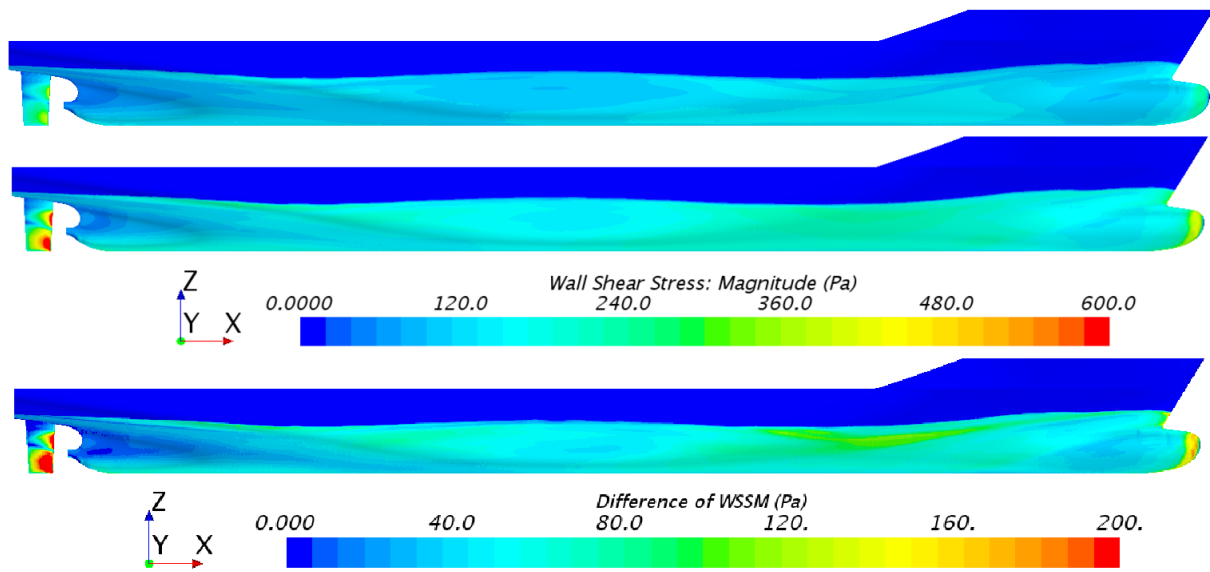


Figure 12. The obtained distribution of τ_w magnitude in SPT for smooth surface condition (upper) and R2 (middle) and the obtained difference of τ_w magnitude between R2 and smooth surface condition (lower)

Figure 13 compares the axial velocity contours at the $y=0$ plane in SPT for smooth surface and R2. The accelerated flow downstream the propeller for R2 condition can be explained by the increase in n due to biofouling, Table 11. In other words, as the self-propulsion points of the fouled cases are achieved at higher propeller rotations due to the negative effect of the hull and propeller fouling, the propeller for R2 condition accelerates the flow more than the smooth condition, as observed by Song^c et al. (2019). This can be noticed in Figure 13, where the dark blue region which characterises more accelerated flow (the flow with higher axial velocity) is larger for surface condition R2 than for smooth surface condition.

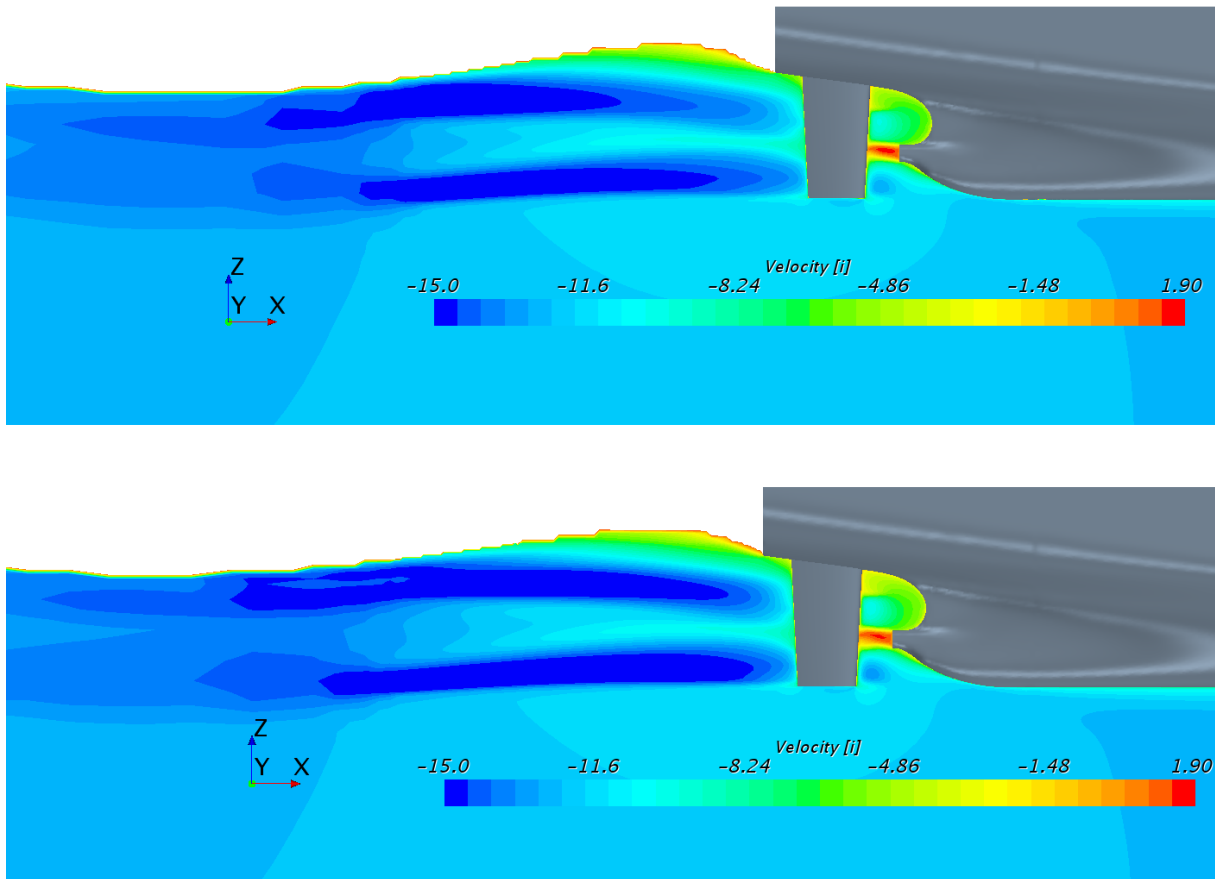


Figure 13. The obtained contours of axial velocity at symmetry plane in SPT for smooth surface (upper) and R2 (lower)

Distribution of dynamic pressure coefficient along the wetted surface of the smooth and fouled (R2) KCS hull (without rudder) is presented in Figure 14. As can be seen from the figure the distributions of dynamic pressure coefficient are similar in the bow and midship region. However in the region of bow and stern shoulder slightly lower values of dynamic pressure coefficients are obtained for smooth surface condition, which means that the pressure gradient is slightly higher for smooth surface condition than for R2 and this can be seen in Figure 14 where the difference of dynamic pressure coefficient obtained for R2 and smooth surface condition is shown. It should be noted that in Figure 14, difference of dynamic pressure coefficient in the stern region is not shown. In order to compare these distributions in more detail at the stern part of a hull, Figure 15, only the stern region of the ship is analysed. From this figure, it can be seen that R2 case has smaller pressure magnitudes compared to the smooth condition, i.e. the presence of biofilm reduces the pressure recovery at the stern region. This implies that the effect of biofilm increases the viscous pressure resistance as similarly found by Song et al. (2019).

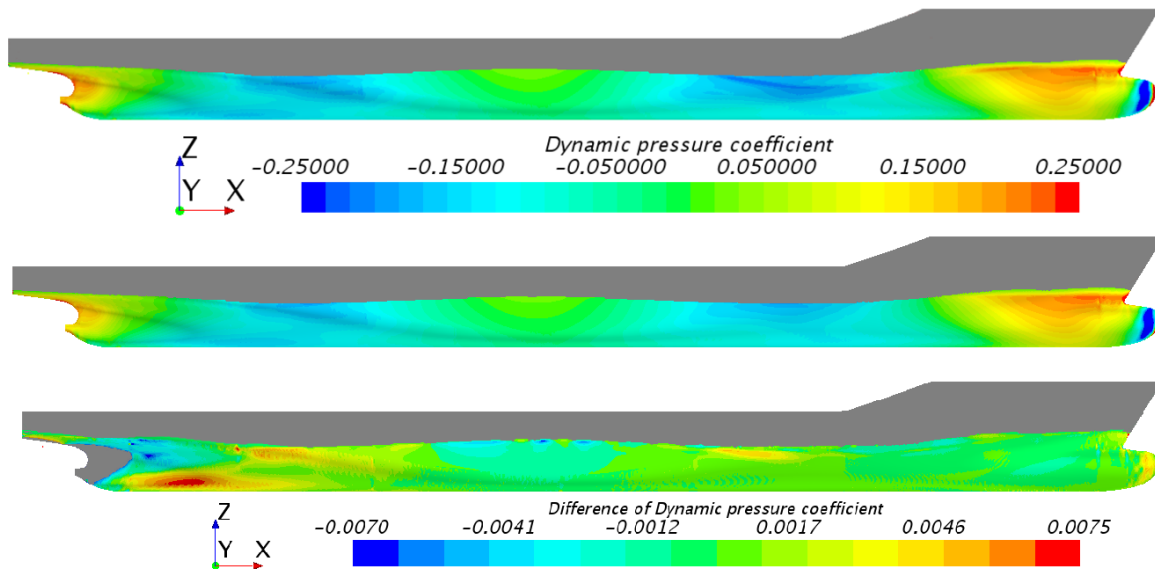


Figure 14. Distribution of dynamic pressure coefficient along the wetted surface of the smooth (upper) and R2 (middle) hull and the obtained difference of dynamic pressure coefficient between R2 and smooth surface condition (lower)

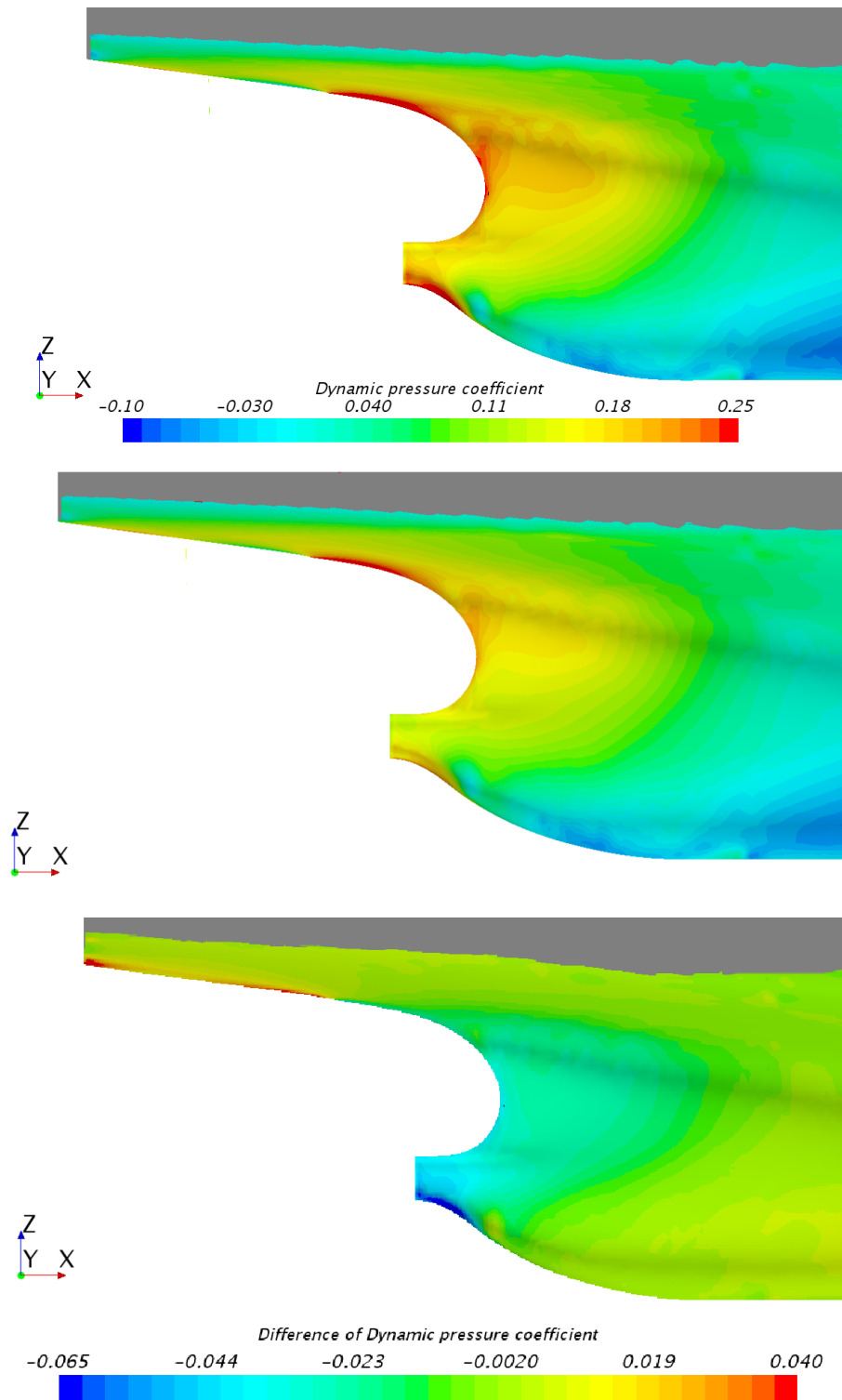


Figure 15. Distribution of dynamic pressure coefficient in the stern region of the smooth (upper left) and R2 (upper right) hull and the obtained difference of dynamic pressure coefficient between R2 and smooth surface condition

Figure 16 compares the pressure coefficients on $y=0$ plane in the smooth and R2 conditions. The presence of biofilm causes the decreases of pressure downstream the hull. This decreased pressure below the free surface results in reduced wave elevation as shown in Figure 17. This observation is in accordance with the findings of recent studies (Farkas et al., 2019, Song^c et al., 2019).

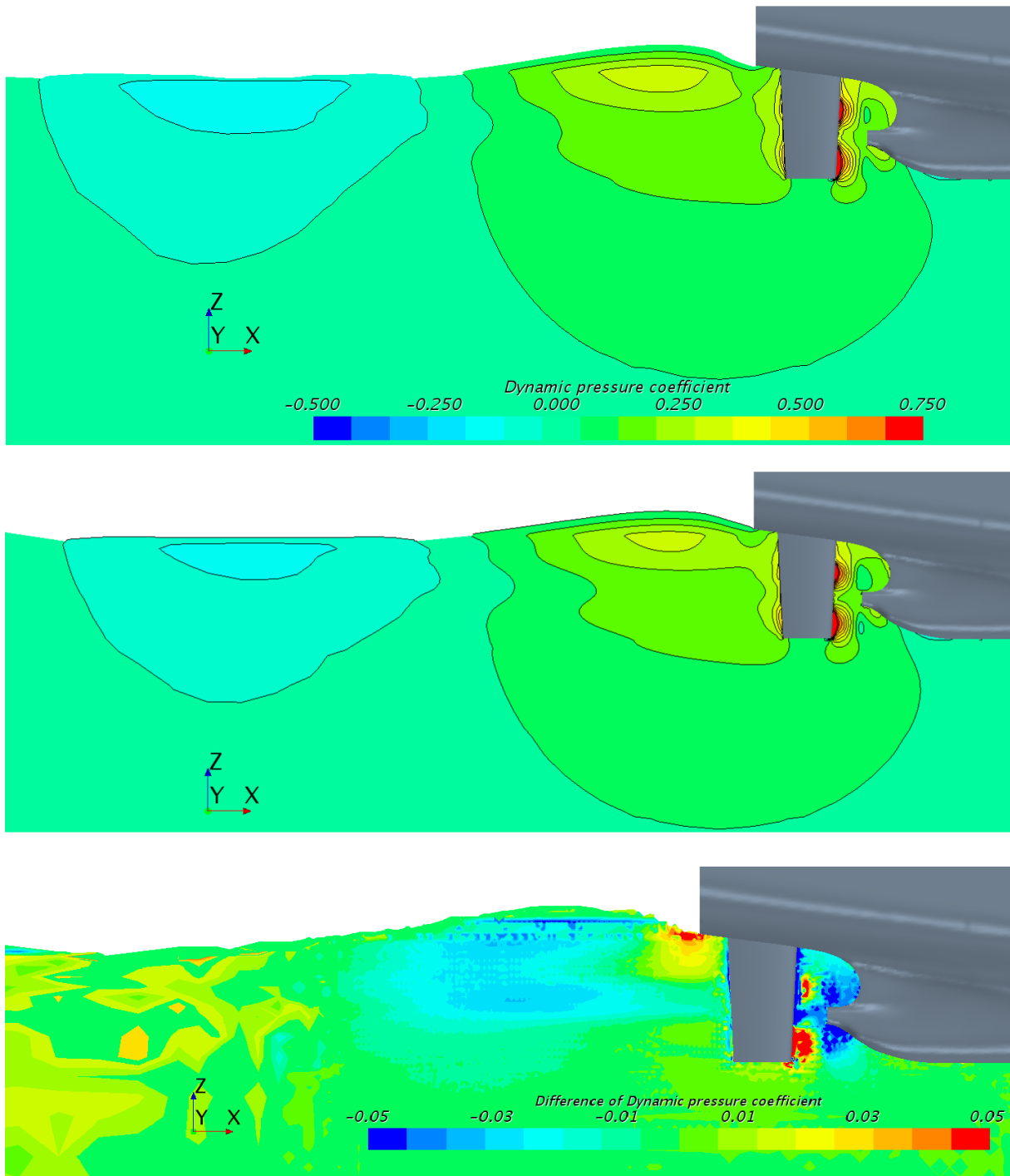


Figure 16. Distribution of dynamic pressure coefficient downstream to the smooth hull (upper) and fouled hull, R2 (middle) and the obtained difference of dynamic pressure coefficient between R2 and smooth surface condition

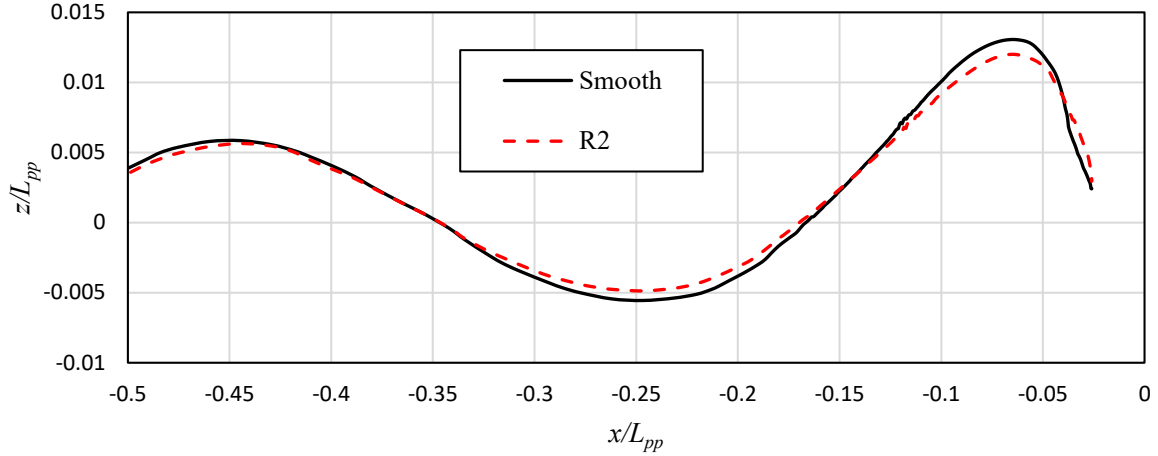


Figure 17. The impact of biofilm on the wave elevation, at $y=0$ plane

Conclusion

CFD model for the assessment of the impact of biofilm on propulsion characteristics has been presented. The impact of biofilm on the propulsion characteristics is evaluated for a benchmark container ship KCS, utilizing the roughness function models proposed in (Farkas^b et al., 2018), which are based on the roughness function values given in (Schultz et al., 2015). Roughness function models are validated and proven to be applicable for the assessment of the impact of biofilm on the flow around any arbitrary body (Farkas^b et al., 2018, Farkas et al., 2019). Roughness function models are implemented within the wall function of the solver and used for the numerical simulation of the open water and self-propulsion tests. Thus, the boundary condition on the propeller and hull surface represents the surface fouled with biofilm.

The GCI method is used for the verification study and the numerical uncertainties have been estimated. Both spatial and temporal convergence studies are performed to assess adequate grid spacings and time steps. Thereafter, the obtained open water and self-propulsion characteristics for the smooth surface condition are validated by the comparison with the experimentally obtained results. The experimentally obtained results are extrapolated to the full-scale values using ITTC 1957 Performance Prediction Method, as numerical simulations are performed at the full scale. The obtained numerical results show satisfactory agreement with the experimental results and obtained RD are in agreement with previously published studies (Castro et al., 2011).

After the verification and validation studies, the impact of biofilm on the open water characteristics is analysed for eight surface conditions. Results have demonstrated that the presence of biofilm causes a decrease in K_T and an increase in K_Q , which leads to a significant decrease in η_O from -2.8% up to -9.4% for R2, depending on J . These changes are more pronounced at higher J , since at the higher J the resultant velocities of the flow approaching the propeller blade section are higher, and this leads to higher U_r values. Due to higher U_r values, higher k^+ values are obtained at the propeller surfaces and

therefore the effect of biofilm is more pronounced. This finding corresponds with the prediction made by Kresic et al (1983), where the authors obtained a significant loss of η_o , even in the presence of small roughness.

The impact of biofilm on the propulsion characteristics is analysed through two approaches, constant speed and constant P_D . Thus, if the ship speed is maintained, i.e. $v=24$ kn, the obtained increase in P_D ranges from 1.4% for R7 up to 36.3% for R2, and the increase in n ranges from 0.1% for R7 up to 4.8% for R2. This detrimental effect of biofilm on P_D can be attributed to several effects. Thus, the presence of biofilm causes the increase in R_T , i.e. P_E from 0.5% for R7 up to 25.8% for R2, and the decrease in η_o as already mentioned. However, besides these two detrimental effects, biofilm also causes changes in the propeller operating point. The presence of biofilm causes the decrease in $1-w$ up to -3.7% for R2 and due to the increase in n , J is reduced significantly and for R2 decrease in J is equal to -8.1%. This decrease is unfavourable, as marine propellers would not operate with the optimum J . It is found that the influence of the biofilm on $1-t$ and η_R values is rather low and this finding is in accordance with assumptions made by Townsin et al. (1985). However, it should be noted that biofilm represents soft fouling with relatively low fouling rate and in order to make a definite conclusion regarding the influence of biofouling on the $1-t$ and η_R values, additional studies should be performed. Even though, a positive impact of biofilm on η_H is noticed, η_p is significantly reduced and this reduction ranges from -0.9% for R7 up to -7.8% for R2. Obviously, the detrimental effect of biofilm on the open water characteristics and shifting of the operating point is more dominant than the positive impact of biofilm on η_H .

The impact of biofilm on the speed reduction with a constant P_D is assessed for two different reference speeds, i.e. the design speed (24 kn) and the slow steaming speed (19 kn). For the design speed, Δv ranges from -0.4% for R7 up to -8.4% for R2, while for slow steaming speed, Δv ranges from 0% for R7 up to -8.6% for R2. It is found that the effect of biofilm at slow steaming speed for surface condition R7 is negligible, as k^+ values along the hull are mostly below a threshold value, i.e. the flow around the hull is in hydraulically smooth regime. Besides speed reduction for a constant P_D equal to P_D obtained for smooth surface condition, the biofilm causes the change of propeller curve. Thus, for fouled hull and propeller, propeller curve is shifted to the left, towards lower values of n , i.e. propeller curve behaves as heavy loaded propeller curve. This leads to an increase in Q and the decrease in n at the reduced speed for fouled ship, when compared to the design speed for unfouled ship. This is very important, as the engine may not be able to deliver P_D , due to an increase in Q . Therefore, either the ship speed would have to be reduced even more and the engine would deliver lower P_D when compared to P_D for smooth surface condition, or additional gear system would be needed, which is not desirable.

A detailed analysis of the flow around the self-propelled KCS hull has led to several conclusions. Thus, it is shown that the presence of biofilm causes the increase of boundary layer thickness, the increase in the τ_w values along the hull as well as the increase in turbulence. All of this leads to an increase in R_F leading to an increase in R_T . By comparing the axial velocity

distributions around propeller obtained for smooth surface condition and R2, it is found that the fouled propeller accelerates the flow more than unfouled propeller in order to maintain the speed. Furthermore, it is found that the presence of biofilm causes the reduction of pressure recovery at the stern and higher pressure gradients at the rudder surface.

This paper has shown that the fouling with the biofilm should not be ignored and that the presence of biofilm can cause extremely detrimental effects on the ship hydrodynamic characteristics. Thus, it is shown that the fouling with biofilm can cause a significant increase in P_D and consequently an increase in fuel consumption or decrease in ship speed.

Using the approach presented within this paper, several valuable insights have been presented containing the effect of biofilm on the ship propulsion characteristics, speed reduction, as well as the flow characteristics around the ship. These insights can be valuable in the assessment of the required power, fuel consumption as well as the greenhouse gas emissions of ships and propellers fouled with the biofilm. Nevertheless, it is still challenging to relate these specific fouling conditions of ship and propeller with real ships operating in the world seas. The fouling on the ship hull and propeller is dependent on various factors including sailing area (salinity, water temperature, sunlight, existing flora and fauna), frequency of changes in sailing regions, ratio of sailing and staying in harbour times, the applied AF coatings, etc. Therefore, the future studies related to biofouling problems are needed for better understanding of time-dependent biofouling growth of the ship hull and propeller surfaces. One of the initial steps into development of time-dependent biofouling growth model is presented in (Uzun et al., 2019). The further investigation related to biofouling problems is valuable, because the potential benefits of the optimization of the maintenance schedule are not only related to economic benefits, but to environmental ones as well.

References

Adland, R, Cariou, P, Jia, H and Wolff, FC., 2018. The energy efficiency effects of periodic ship hull cleaning. *Journal of Cleaner Production*, 178, pp. 1-13.

Bertram, V. Added Power in Waves – Time to Stop Lying (to Ourselves), In: 1st Hull Performance & Insight Conference (ed. V Bertram), Castello di Pavone, Italy, 5-13 April 2016, pp. 282-291.

Bertram, V. Some Heretic Thoughts on ISO 19030, In: 2nd Hull Performance & Insight Conference (ed. V Bertram), Ulrichshusen, Germany, 27-29 March 2017, pp. 4-11.

Carlton, J. *Marine Propellers and Propulsion*, 2007, Butterworth-Heinemann, Linacre House, Jordan Hill, Oxford OX2 8DP, 30 Corporate Drive, Suite 400, Burlington, MA 01803, USA

Castro, AM., Carrica, PM and Stern, F., 2011. Full scale self-propulsion computations using discretized propeller for the KRISO container ship KCS. *Computer & fluids*, 51(1), pp. 35-47.

Coraddu, A., Lim, S., Oneto, L., Pazouki, K., Norman, R., & Murphy, A. J., 2019. A novelty detection approach to diagnosing hull and propeller fouling. *Ocean Engineering*, 176, pp. 65-73.

Davidson, I. C., Brown, C. W., Sytsma, M. D., Ruiz, G. M., 2009. The role of containerships as transfer mechanisms of marine biofouling species. *Biofouling*, 25(7), pp. 645-655.

Demirel, Y. K., Khorasanchi, M., Turan, O., Incecik, A., Schultz, M. P., 2014. A CFD model for the frictional resistance prediction of antifouling coatings. *Ocean Engineering*, 89, pp. 21-31.

Demirel, Y. K., Song, S., Turan, O., & Incecik, A., 2019. Practical added resistance diagrams to predict fouling impact on ship performance. *Ocean Engineering*, 186, pp. 106112.

Demirel^a, Y. K., Uzun, D., Zhang, Y., Fang, H. C., Day, A. H., Turan, O., 2017. Effect of barnacle fouling on ship resistance and powering. *Biofouling*, 33(10), pp. 819-834.

Demirel^b, YK, Turan, O and Incecik A., 2017. Predicting the effect of biofouling on ship resistance using CFD. *Applied Ocean Research*, 62, pp. 100-118.

Farkas, A, Degiuli, N and Martić, I., 2017. Numerical investigation into the interaction of resistance components for a series 60 catamaran. *Ocean Engineering*, 146, pp. 151-169.

Farkas^a, A, Degiuli, N and Martić, I., 2018. Assessment of hydrodynamic characteristics of a full-scale ship at different draughts. *Ocean Engineering*, 156, pp. 135-152.

Farkas^b, A, Degiuli, N and Martić, I., 2018. Towards the prediction of the effect of biofilm on the ship resistance using CFD. *Ocean Engineering*, 167, pp. 169-186.

Farkas, A., Degiuli, N., Martić, I., 2019. Impact of biofilm on the resistance characteristics and nominal wake. Proceedings of the Institution of Mechanical Engineers Part M-Journal of Engineering for the Maritime Environment, Online First, 1475090219862897.

Flack, K. A., Schultz, M. P., Connelly, J. S., 2007. Examination of a critical roughness height for outer layer similarity. Physics of Fluids, 19(9), pp. 095104.

Flack, KA and Schultz, MP., 2014. Roughness effects on wall-bounded turbulent flows. Physics of Fluids, 26(10), pp. 101305.

Gundermann, D and Dirksen, T. A Statistical Study of Propulsion Performance of Ships and the Effect of Dry Dockings, Hull Cleanings and Propeller Polishes on Performance, In: 1st Hull Performance & Insight Conference (ed. V Bertram), Castello di Pavone, Italy, 13-15 April 2016, pp. 282-291.

Hydrex Underwater Technology. The slime factor, http://ec.europa.eu/environment/life/project/Projects/index.cfm?fuseaction=home.showFile&rep=file&fil=ECOTEC_The_Slime_Factor.pdf, 2010., accessed 11 October 2019.

International Maritime Organisation (IMO). Air pollution and energy efficiency. MEPC 63.4.8., 2011.

International Organization for Standardization (ISO). ISO 19030-1:2016 Ships and marine technology-Measurement of changes in hull and propeller performance-Part 1: General principles, 2016.

ITTC Specialist Committee on Surface Treatment. Final report and recommendation to the 26th ITTC. Proceedings of 26th ITTC – Volume II, Rio de Janeiro, Brazil, 2011.

Kim, W. J., Van, S. H., Kim, D. H., 2001. Measurement of flows around modern commercial ship models. Experiments in Fluids, 31(5), pp. 567-578.

Koboević, Ž., Bebić, D., Kurtela, Ž., 2019. New approach to monitoring hull condition of ships as objective for selecting optimal docking period. *Ships and Offshore Structures*. 14(1), pp. 95-103.

Kresic, M., Haskell, B., 1983. Effects of propeller design-point definition on the performance of a propeller/diesel engine system with regard to in-service roughness and weather conditions. *Society of Naval Architects and Marine Engineers-Transactions*, 91, pp. 195-224.

Monty, J. P., Dogan, E., Hanson, R., Scardino, A. J., Ganapathisubramani, B., Hutchins, N., 2016. An assessment of the ship drag penalty arising from light calcareous tubeworm fouling. *Biofouling*, 32(4), pp. 451-464.

Naval Ships' Technical Manual, 2002. Waterborne underwater hull cleaning of navy ships. S9086-CQ-STM-010/CH-081R5. Naval Sea Systems Command.

NMRI. Tokyo 2015 A Workshop on CFD in Ship Hydrodynamics, <http://www.t2015.nmri.go.jp/kcs.html> (2015, accessed 11 October 2019).

Nurioglu, AG, Esteves, ACC and de With, G., 2015. Non-toxic, non-biocide-release antifouling coatings based on molecular structure design for marine applications. *Journal of Materials Chemistry B*, 3(32), pp. 6547-6570.

Owen, D, Demirel, YK, Oguz, E, Tezdogan, T and Incecik, A., 2018. Investigating the effect of biofouling on propeller characteristics using CFD. *Ocean Engineering*, 159, pp. 505-516.

Park, J., Kim, B., Shim, H., Ahn, K., Park, J. H., Jeong, D., Jeong, S., Hull and Propeller Fouling Decomposition and Its Prediction based on Machine Learning Approach. In: 3rd Hull Performance & Insight Conference (ed. V Bertram), Redworth, UK, 12-14 March 2018, pp. 20-26.

Schultz, M. P., 2000. Turbulent boundary layers on surfaces covered with filamentous algae. *Journal of Fluids Engineering*, 122(2), pp. 357-363.

Schultz, MP, Finlay, JA, Callow, ME and Callow, JA., 2003. Three models to relate detachment of low form fouling at laboratory and ship scale. *Biofouling*, 19(S1), pp. 17-26.

Schultz, MP, Walker, JM, Steppe, CN and Flack, KA., 2015. Impact of diatomaceous biofilms on the frictional drag of fouling-release coatings. *Biofouling*, 31(9-10), pp. 759-773.

Silva, E. R., Ferreira, O., Ramalho, P. A., Azevedo, N. F., Bayón, R., Igartua, A., Bordado, J. C., Calhorda, M. J., 2019. Eco-friendly non-biocide-release coatings for marine biofouling prevention. *Science of the Total Environment*, 650, pp. 2499-2511.

Song^a, S., Demirel, Y. K., & Atlar, M., 2020. Effect of biofouling on ship self-propulsion performance. *Applied Ocean Research*, 94, 102006.

Song^b, S., Demirel, Y. K., & Atlar, M., An investigation into the effect of biofouling on full-scale propeller performance using CFD. In 38th International Conference on Ocean, Offshore & Arctic Engineering, Glasgow, UK, 9-14 June, 2019.

Song^c, S., Demirel, Y. K., Atlar, M., 2019. An investigation into the effect of biofouling on the ship hydrodynamic characteristics using CFD. *Ocean Engineering*, 175, pp. 122-137.

Speranza, N., Kidd, B., Schultz, M. P., Viola, I. M., 2019. Modelling of hull roughness. *Ocean Engineering*, 174, pp. 31-42.

Stojanović, I., Farkas, A., Alar, V., Degiuli, N., 2019. Evaluation of the Corrosion Protection of Two Underwater Coating Systems in a Simulated Marine Environment. *JOM-The Journal of The Minerals, Metals & Materials Society (TMS)*, First Online, pp. 1-9.

Tarełko, W., 2014. The effect of hull biofouling on parameters characterising ship propulsion system efficiency. *Polish Maritime Research*, 21(4), pp. 27-34X.

Terziev, M., Tezdogan, T., Oguz, E., Gourlay, T., Demirel, Y. K., Incecik, A., 2018. Numerical investigation of the behaviour and performance of ships advancing through restricted shallow waters. *Journal of Fluids and Structures*, 76, pp.185-215.

Tezdogan, T, Demirel, YK, Kellet, P, Khorasanchi, M, Incecik, A and Turan, O., 2015. Full-scale unsteady RANS CFD simulations of ship behaviour and performance in head seas due to slow steaming. *Ocean Engineering*, 97, pp. 186-206.

Tezdogan, T., & Demirel, Y. K., 2014. An overview of marine corrosion protection with a focus on cathodic protection and coatings. *Brodogradnja*, 65, pp. 49–59.

Townsin, R. L., Spencer, D. S., & Mosaad, M., 1985. Rough propeller penalties. *Society of Naval Architects and Marine Engineers-Transactions*, 93, pp. 165-187.

Tzamaloukas, A., Glaros, S., Bikli, K. Different Approaches in Vessel Performance Monitoring, Balancing Accuracy, Effectiveness & Investment Aspects, from the Operator's Point of View. In: 3rd Hull Performance & Insight Conference (ed. V Bertram), Redworth, UK, 12-14 March 2018, pp. 149-161.

Uzun, D., Demirel, Y. K., Coraddu, Turan, O., 2019. Time-dependent biofouling growth model for predicting the effects of biofouling on ship resistance and powering. *Ocean Engineering*, 191, 106432.

van Ballegooijen, E., Helsloot, T., An Approach to Monitor the Propeller Separately from the Hull, In: 4th Hull Performance & Insight Conference (ed. V Bertram), Gubbio, Italy, 6-8 May 2019, pp. 50-55.

Woods, C. M., Floerl, O., Jones, L., 2012. Biosecurity risks associated with in-water and shore-based marine vessel hull cleaning operations. *Marine pollution bulletin*, 64(7), pp. 1392-1401.

Yeginbayeva, I. A., Granhag, L., Chernoray, V., 2019. Review and historical overview of experimental facilities used in hull coating hydrodynamic tests. *Proceedings of the Institution of Mechanical Engineers Part M-Journal of Engineering for the Maritime Environment*, 233(4), pp. 991-999.